

M.B. Khanvilkar<sup>1,2</sup>, A.K. Nikumbh<sup>1</sup>, R.A. Pawar<sup>1</sup>, N.J. Karale<sup>1</sup>, D.V. Nighot<sup>1</sup>,  
R.C. Ambare<sup>2</sup>, P.A. Nagwade<sup>1</sup>, M.D. Sangale<sup>1</sup>, G.S. Gugale<sup>1</sup>, S.B. Misal<sup>1</sup>

## Preparation and Characterization of Nanosized Substituted Perovskite Compounds with Orthorhombic Structure

<sup>1</sup>Department of Chemistry, Savitribai Phule Pune University (Formerly University of Pune), Ganeshkhind, Pune, India, [mb.khanvilkar@gmail.com](mailto:mb.khanvilkar@gmail.com)

<sup>2</sup>K.M.C.College, Khopoli, Tal-Khalapur, Dist. Raigad, India, [revanambare@gmail.com](mailto:revanambare@gmail.com)

In this work, five substituted perovskite such as  $(\text{Gd}_{0.9}\text{Sr}_{0.1})\text{Mn}_{0.8}\text{Co}_{0.2}\text{O}_3$ ,  $\text{Tb}_{0.8}\text{Sr}_{0.2}\text{FeO}_3$ ,  $\text{Gd}_{0.6}\text{Sr}_{0.4}\text{RuO}_3$ ,  $\text{SrCe}_{0.95}\text{Y}_{0.05}\text{O}_3$ , and  $\text{Mn}_{0.6}\text{Co}_{0.4}\text{SnO}_3$  were synthesized by tartrate and hydroxide precursor method. The resulting samples were characterized by inductively coupled plasma spectroscopy, energy dispersive X-ray analysis, infrared spectroscopy, thermal analysis, X-ray powder diffraction, transmission electron microscope (TEM), selected field of electron diffraction (SAED), d.c. electrical conductivity, Hall effect, dielectric measurements, and low-temperature magnetization measurements. The X-ray diffraction pattern for all compounds was indicated the formation of single-phase perovskite with orthorhombic structure except  $\text{Tb}_{0.8}\text{Sr}_{0.2}\text{FeO}_3$  and  $\text{Mn}_{0.6}\text{Co}_{0.4}\text{SnO}_3$  perovskite. These compounds showed a cubic and rhombohedral structure, respectively. The lattice parameter and the unit cell volume slightly decreased as ionic radii decrease in agreement with the lanthanide contraction. The average size of cation  $\langle R_A \rangle$ , mismatch factor ( $\sigma^2$ ), and tolerance factor ( $t$ ) gives the combined effects of disorder and inhomogeneity in these compounds. The average particle size determined from TEM was in the range of 22 to 77 nm for all compounds. The different lattice planes in the SAED pattern were assigned and these were in agreement with the single crystallographic phase of these perovskites. The temperature dependence of electrical conductivity for all compounds showed a definite break in 500 K to 610 K. except the  $\text{Gd}_{0.6}\text{Sr}_{0.4}\text{RuO}_3$  compound, which corresponds to semiconducting behavior. While the  $\text{Gd}_{0.6}\text{Sr}_{0.4}\text{RuO}_3$  sample shows a metallic-like semiconductor. The thermoelectric power and Hall effect measurements for all compounds were n-type semiconductivity except the  $\text{SrCe}_{0.95}\text{Y}_{0.05}\text{O}_3$  compound. It showed p-type semiconductivity. The frequency dependence of the dielectric constant and dielectric loss in these substituted perovskites were discussed using the Maxwell-Wagner model. Magnetic studies showed that the thermo-magnetic (ZFC and FC measurement) irreversibility for all compounds.

**Keywords:** nanosized substituted perovskite, ferromagnetism, electrical conductivity, magnetization, exchange interaction.

Received 20 June 2021; Accepted 25 October 2021.

## Introduction

Perovskites with an  $\text{ABO}_3$  structure have shown great promise in a wide range of applications, including sensors [1-3], solid oxide fuel cells [4-5], ceramic membrane technologies [6, 7], and catalysis [8, 9].

In traditional  $\text{ABO}_3$  Perovskites, the A-site is normally filled by lanthanides, alkali metals, or alkaline earth metals, while the B-site elements are typically first

or second-row transition metals [10-12]. Partial substitution, on the other hand, can occur at the A-site, the B-site, or both the A- and B-sites at the same time ( $\text{A}_{1-x}\text{A}'_x\text{B}_{1-y}\text{B}'_y\text{O}_{3+\delta}$ ); The goal of substitution is to improve or fine-tune physical properties such as thermal stability, chemical stability, electrical conductivity, magnetic effects, catalytic activity, and electrode-electrolyte compatibility in order to increase the commercial utility of perovskite devices.

The magnetic behavior of substituted manganates

depends on the ratio of  $Mn^{3+}/Mn^{4+}$  and is regulated by the A-site cation average radius  $\langle r_a \rangle$  or tolerance factor, which is a geometric factor indicating the degree of distortion of the cubic perovskite structure [13]. Maximum ferromagnetic Curie temperature in  $R_{1-x}A_xMnO_3$  is observed when  $R = La$  and ferromagnetism is observed for  $0.1 < x < 0.5$  with maximum  $T_c$  for  $x = 1/3$  [14-16]. When the  $Mn^{3+}/Mn^{4+}$  ratio in substituted manganates is 1:1, true space charge ordering of the Mn ions is observed at low temperatures ( $x = 0.5$ ). Ferromagnetism and ground-state transition from ferromagnetic to antiferromagnetic transition are suppressed by the charge ordering [17]. The  $Pr_{0.5}Ca_{0.5}Mn_{1-y}Co_yO_3$  series offers a weakening of the inclination to charge order by sufficient substitutions on the manganese sites with other transition metal ions. The incidence of charge ordering state is fully suppressed for  $0.03 \leq y \leq 0.05$ , and an insulator-metal transition exists in the temperature range from 80 to 60 K [18].

$RFeO_3$  ( $R =$  rare earth) has recently become part of the perovskite oxide family with an orthorhombic cell unit. They are insulators with a good anti-ferromagnetic coupling between ions of  $Fe^{3+}$ . This leads to high TN Neel temperature values. For example, for  $GdFeO_3$ ,  $T_N = 657$  K [19].  $SrFeO_3$ , on the other hand, is a TN = 130 K metallic antiferromagnet [20]. It reveals a magnetic helical structure with a magnetic moment of  $3.1 \mu_B$  per ion  $Fe^{4+}$ .  $Fe^{4+}$  ions in  $SrFeO_3$  are normally thought to be in high spin  $3d^4$  condition with three localized electrons in the  $t_{2g}$  band, while the fourth electron is delocalized in a broad  $\sigma^*$  band [21-22].

Ruthenate perovskites such as  $SrRuO_3$ ,  $CaRuO_3$ , and  $LaRuO_3$  have a low resistivity metallic property at room temperature [23], while  $PrRuO_3$  has a semiconducting property [24].  $SrRuO_3$  is ferromagnetic below  $T_c = 160$  K followed by a small shift in Curie temperature resistivity and  $CaRuO_3$  follows a Curie Weiss law with a negative Weiss constant at high temperatures and no resistivity deviations down to 4.3 K [23, 25, 26]. Magnetic measurements have been investigated using the solid solution  $Sr_{1-x}Ca_xRuO_3$ . With the replacement of  $Ca^{2+}$  for  $Sr^{2+}$ , these measurements revealed a decrease in the Curie temperature, suggesting a weakening of the ferromagnetic exchange interaction [27, 28].

The compound  $ACe_{1-x}R_xO_{3-\delta}$  ( $A = Ba$  and  $Sr$ ,  $R =$  rare earth elements) belongs to perovskite-type oxides, which in addition to good oxygen-ion conductivity, exhibit excellent high proton-conducting efficiency [29-31]. The transport properties of these materials generally depend critically on the structure of crystals and chemical stoichiometry. Oxygen conduction results from the movement of oxygen ions between oxygen vacancies that are introduced by the partial substitution of  $R^{3+}$  ions for  $Ce^{4+}$ , while proton conduction occurs when hydrogen dissolves in the lattice through hydroxyl ions that form. A variety of researchers have studied the influence of the dopant on the crystal structure and electrical properties of  $A-Ce_{1-x}R_xO_{3-\delta}$  perovskites ( $A = Ba$  and  $Sr$ , and  $R = Y$ ,  $Nd$ ,  $Gd$ ,  $Yb$ ) [32-34].

Due to dielectric and piezoelectrics, Transition Metal Stannates have wide application. Cadmium stannates have been studied for potential use in solar batteries as transparent electrode materials [35]. Zn, Cu, Cd, Fe, Mn

stannates are semiconductors with the disordered structure of ilmenite and can be prepared under special conditions [36]. Stannate doping ( $ASnO_3$ ) with transition d metal has been studied for the synthesis of cobalt-containing oxide ( $Sr_{1-x}La_xSn_{1-x}Co_xO_3$  [37] and iron-containing oxide  $Sr(Sn_{1-x}Fe_x)O_3$  [38-39]. It was found that the conduction differs from ionic-electronic to electronic form for  $Sr(Sn_{1-x}Fe_x)O_{3-\delta}$  solid solution, with an increasing Fe to Sn ratio. These solid solutions have a cubic structure within the concentration range of  $0.4 < x < 0.9$ .

Recent research [40] has shown that reducing the size to the nanometer range of perovskite particles reduces their magnetization. It is therefore an important issue to increase the magnetization of nanocrystalline perovskite materials. Substituting on the A-site or B-site or both sites is one possible way to improve the magnetic properties or to increase electrical conductivity due to increased oxygen vacancies of  $ABO_3$  perovskites. A new series of substituted perovskite materials are synthesized in this paper with the formula  $Gd_{0.9}Sr_{0.1}Mn_{0.8}Co_{0.2}O_3$ ,  $Tb_{0.8}Sr_{0.2}FeO_3$ ,  $Gd_{0.6}Sr_{0.4}RuO_3$ ,  $SrCe_{0.95}Y_{0.05}O_3$ , and  $Mn_{0.6}Co_{0.4}SnO_3$ , and the effect of the substitution, on the structure, electrical and magnetic properties of these perovskites are studied.

## I. Experimental

### 1.1. Synthesis of precursors

#### 1.1.1. Gadolinium-strontium-manganese-cobalt tartrate fourteen hydrate, $(Gd_{0.9}Sr_{0.1})Mn_{0.8}Co_{0.2}(C_4H_4O_6)_{2.5} \cdot 14H_2O$

This precursor was prepared in double-distilled water using the co-precipitation method by taking  $Gd(NO_3)_3 \cdot 6H_2O$  (2.9272 g),  $SrCl_2 \cdot 6H_2O$  (0.5765 g),  $MnCl_2 \cdot 4H_2O$  (2.2924 g) and  $CoCl_2 \cdot 6H_2O$  (0.2643 g). The medium's pH was changed to a sufficiently low value ( $pH < 5$ ). A magnetic stirrer was used to stir the solution vigorously. Ammonium tartrate (4.4774 g in 25 mL distilled water) was then applied to this solution slowly until a permanent precipitate occurred. To get more homogeneous, stoichiometric, fine-grained powders, acetone was added in similar quantities. Pink in color was the resulting precipitate of  $(Gd_{0.9}Sr_{0.1})Mn_{0.8}Co_{0.2}(C_4H_4O_6)_{2.5} \cdot 14H_2O$ . The solution was filtered for 30 minutes after being stirred. For  $Gd^{3+}$ ,  $Sr^{2+}$ ,  $Mn^{2+}$ , and  $Co^{2+}$ , whose absence ensured absolute co-precipitation, the filtrate was tested. To accelerate the drying, the precipitate was washed with cold distilled water and then with acetone. At room temperature, it was air-dried.

By following the procedure given above, other tartrate/hydroxide coprecipitates were prepared. Below are the additional related information summarized.

#### 1.1.2. Terbium - strontium - iron tartrate two hydrate $Tb_{0.8}Sr_{0.2}Fe(C_4H_4O_6)_{2.5} \cdot 2H_2O$

To avoid air oxidation of  $Fe^{2+}$  ion, 0.5195 g iron metal powder (electrolytic) was dissolved in 5mL concentrated hydrochloric acid in a three-neck flask under a stream of dry nitrogen atmosphere. The solution

on a low flame was then evaporated to dryness. The resulting crystalline green ferrous chloride residue was dissolved in double-distilled water (50 mL). 1.3354 g  $\text{Tb}(\text{NO}_3)_3 \cdot 6\text{H}_2\text{O}$  (10 mL D.W.) and 2.2157 g  $\text{SrCl}_2 \cdot 6\text{H}_2\text{O}$  (10 mL D.W.) were combined with this solution and placed into a flask (500 mL). It was applied slowly with stirring and to this ammonium tartrate solution (4.2338 g in 50 mL distilled water) was added, till a permanent precipitate occurred. It obtained a light green-colored precipitate. The precipitate was filtered and washed at room temperature with distilled water and acetone, followed by air drying.

### 1.1.3. Gadolinium - strontium - ruthenium tartrate four hydrates $\text{Gd}_{0.6}\text{Sr}_{0.4}\text{Ru}(\text{C}_4\text{H}_4\text{O}_6)_3 \cdot 4\text{H}_2\text{O}$

This precursor was prepared in double-distilled water by taking  $\text{Gd}(\text{NO}_3)_3 \cdot 6\text{H}_2\text{O}$  (0.8629 g),  $\text{SrCl}_2 \cdot 6\text{H}_2\text{O}$  (2.0393 g), and  $\text{RuCl}_3 \cdot 3\text{H}_2\text{O}$  (2.00 g). (50 mL). It was applied slowly with stirring and to this ammonium tartrate solution (4.6195 g in 50 mL distilled water) was added until a permanent precipitate occurred. The gray-colored precipitate was collected. To accelerate the drying, the precipitate was filtered and washed with distilled water and then with acetone. It was air-dried at room temperature.

### 1.1.4. Strontium - cerium - yttrium tartrate three hydrates $\text{Sr Ce}_{0.95}\text{Y}_{0.05}(\text{C}_4\text{H}_4\text{O}_6)_{2.5} \cdot 3\text{H}_2\text{O}$

The co-precipitation method was used to prepare this precursor by taking  $\text{SrCl}_2 \cdot 6\text{H}_2\text{O}$  (2.6273 g),  $\text{Ce}(\text{NO}_3)_3 \cdot 6\text{H}_2\text{O}$  (3.0086 g), and  $\text{Y}(\text{NO}_3)_3 \cdot 5\text{H}_2\text{O}$  (0.2698 g) into double distilled water. To this ammonium tartrate solution (4.0510 g dissolved in 25 mL distilled water) was added slowly with stirring, till a permanent white precipitate occurred. The precipitate has been filtered and washed at room temperature with distilled water and dry air.

### 1.1.5. Manganese - Cobalt - tin hydroxide, $\text{Mn}_{0.6}\text{Co}_{0.4}\text{Sn}(\text{OH})_6$

In 5 mL of concentrated hydrochloric acid (HCl), 2.0214 g of  $\text{SnCl}_2 \cdot 2\text{H}_2\text{O}$  was dissolved and boiled to form a transparent solution. Dilute the solution to 25 mL with distilled water.

$\text{MnCl}_2 \cdot 4\text{H}_2\text{O}$  (1.0638 g) and  $\text{CoCl}_2 \cdot 6\text{H}_2\text{O}$  (0.8526 g) were dissolved in 10 mL of distilled water in another beaker. Then above  $\text{SnCl}_2$  solution was thoroughly mixed with these solutions. The reagent grade ammonia solution (0.5M  $\text{NH}_3$ ) was added drop-wise to this solution until the precipitation is complete. A magnetic stirrer was used to stir the solution vigorously. The pH of the medium was maintained at  $\leq 8$ . The grey precipitate was subsequently digested for one hour. To obtain content free of chloride ions, the solution was filtered and washed with diluted ammonia solution. At an ambient temperature, the precipitate was then dried and ground with the aid of the agate mortar. The powder sample obtained was restored using desiccators.

## 1.2. Synthesis of nanosized substituted perovskite compounds

In a platinum crucible under a static air atmosphere, the above precursors were decomposed and held slowly

at 700 °C for two hours and then slowly cooled down to room temperature (30 °C/Min). This thermal treatment was adequate for the full decomposition of precursors to be achieved. The obtained powder was polycrystalline. This sample was then re-grounded for another two hours and re-calcined at the same temperature. The furnace was turned off and at room temperature, the sample was removed. In desiccators, substituted perovskite samples such as  $(\text{Gd}_{0.9}\text{Sr}_{0.1})\text{Mn}_{0.8}\text{Co}_{0.2}\text{O}_3$ ,  $\text{Tb}_{0.8}\text{Sr}_{0.2}\text{FeO}_3$ ,  $\text{Gd}_{0.6}\text{Sr}_{0.4}\text{RuO}_3$ ,  $\text{SrCe}_{0.95}\text{Y}_{0.05}\text{O}_3$  and  $\text{Mn}_{0.6}\text{Co}_{0.4}\text{SnO}_3$  have been restored.

## 1.3 Sample Characterization.

Microanalytical methods have been used to carry out the basic analysis of carbon and hydrogen. An inductively coupled plasma spectrometer (ICP-AES instrument ARCOS from M/S. Spectro Germany) and an Energy Dispersive X-ray Analysis (EDS) on SEM PHILIPS XL 30 CP were used for the metal analysis of the sample. For this analysis, duplicate samples were used. Infrared spectra of the precursor were recorded using KBR pellets in the region of 4000 - 450  $\text{cm}^{-1}$  on the Perkin-Elmer 1600 series FTIR spectrophotometer. On a Mettler Toledo 850 instrument, the TGA and DTA were recorded.

The X-ray diffraction pattern (XRD) was obtained at room temperature using a Siemens D 500 diffractometer with  $\text{CuK}\alpha$  radiation ( $\lambda = 1.5418 \text{ \AA}$  and  $\theta = 20 - 80^\circ$ ). On a JEOL-2010 transmission electron microscope, working at an accelerating voltage of 208 kV, transmission electron microscopy (TEM) and corresponding selected area electron diffraction (SAED) pattern were carried out. TEM samples were dispersed by dispersing in 2-propanol. The amorphous carbon film supported on the copper grid was deposited with one or two drops of this solution containing synthesized nano oxides and allowed to dry in the air at room temperature. It determined the average particle size and the crystalline phase of the samples. The procedure used for the measurements of d. c. electrical conductivity and thermoelectric power measurements were identical to those reported in the literature [41]. Measurements of the Hall effect of the samples were analyzed using an ECOPIA instrument (HMS 3000) with a constant magnetic field of 5 Tesla ( $\tau$ ). A HIOKI model 3532-50 LCR Hi Tester (frequency range from 100 Hz to 5 M Hz) at room temperature was used to study the dielectric properties of the substituted perovskite nano oxides at room temperature.

A SQUID magnetometer was used to investigate the magnetic behavior of the samples (Quantum Design MPMS-55). In the 100 Oe field, sample magnetization was tested for heating through the temperature range  $5 < T(\text{K}) < 325$  and after cooling the sample both in the measuring field (field cooling-FC) and in the absence of the applied field (zero-field cooling - ZFC). The magnetization was also measured at room temperature as a function of the field is applied. Data were collected in a field of 50 k Oe in decreasing and increasing fields cooling from the paramagnetic phase to the selected temperature. The measurement of magnetic hysteresis was also studied at room temperature using the vibrating sample magnetometer PAREG and G model no.4508 with an applied field of up to 20 k Oe.

## II. Results and discussion

### 2.1. Characterization of precursors

The basic study of tartrate precursors was performed in percent wt (elemental analysis) for Gadolinium – strontium – manganese Cobalt tartrate,  $Gd_{0.9}Sr_{0.1}Mn_{0.8}Co_{0.2}(C_4H_4O_6)_{2.5} \cdot 14H_2O$ ; (C, cal.14.49 and found 15.04; H cal.4.59 and found 4.28 ;Gd, cal.17.09 and found 16.81; Sr, cal.1.06 and found 1.48; Mn, cal.5.31 and found 5.34; Co, cal. 1.42 and found 1.8); for terbium-strontium-iron tartrate,  $Tb_{0.8}Sr_{0.2}Fe(C_4H_4O_6)_{2.5} \cdot 2H_2O$ ; (C, cal.19.80 and found 19.43; H, cal.2.31 and found 2.42; Tb, cal.20.96 and found 21.72; Sr, cal.2.89 and found 2.58; Fe, cal. 9.20 and found 8.91); for Gadolinium-strontium-ruthenium tartrate,  $Gd_{0.6}Sr_{0.4}Ru(C_4H_4O_6)_3 \cdot 4H_2O$ . (C, cal.19.29 and found 18.83; H cal.2.68 and found 2.32 ; Gd, cal.12.64 and found 13.03; Sr, cal.4.69 and found 4.93; Ru, cal. 13.54 and found 13.17); for Strontium-cerium-yttrium tartrate,  $SrCe_{0.95}Y_{0.05}(C_4H_4O_6)_{2.5} \cdot 3H_2O$  (C, cal.18.48 and found 19.02; H cal.2.46 and found 2.65; Sr, cal.13.49 and found 12.98; Ce, cal. 20.50 and found 20.02; Y, cal. 0.68 and found 0.64); for manganese-cobalt-tin oxyhydroxide,  $Mn_{0.6}Co_{0.4}Sn(OH)_6$  (H cal.2.16 and found 2.61 ; Mn, cal.11.89 and found 12.23; Co, cal.8.50 and found 8.91; Sn, cal.42.82 and found 43.10).

The infrared spectrum of these precursors showed the band assigned to the water of crystallization at  $3362\text{ cm}^{-1}$ , and the intense band due to  $\nu_{asy}$ . at  $1598\text{ cm}^{-1}$  (C=O) and bands at  $1411\text{ cm}^{-1}$  and  $1238\text{ cm}^{-1}$  due to  $\nu_{sy}$ . (C-O). These values indicate the presence of coordinated carboxylate groups. These precursors were assigned to a chain-like polymeric octahedral structure [42, 43]. Measuring magnetic susceptibility at room temperature confirms the precursor's paramagnetic existence, except for strontium-cerium-yttrium tartrate,  $(SrCe_{0.95}Y_{0.05}(C_4H_4O_6)_{2.5} \cdot 3H_2O)$ , which is diamagnetic in nature.

The Manganese-cobalt-tin hydroxide infrared spectrum showing broadband at  $\sim 3348\text{ cm}^{-1}$  corresponds to the presence of -OH stretching vibration and bending vibration of water molecules. The existence of more than one hydroxyl type is also evident from the multiplicity of  $847 - 1411\text{ cm}^{-1}$  bands resulting from the Sn-OH group's deformation vibration having some ionic character. For each transition metal oxyhydroxyl stannate,  $\nu_{Sn-O}$  vibrations have been reported at  $\sim 521\text{ cm}^{-1}$ , suggesting a six-coordinate setting for the metal ions [44].

TGA – DTA analysis was conducted to evaluate the thermal properties of the obtained samples. Fig. 1(a) to (e) show the simultaneous TGA and DTA curves in normal air of  $(Gd_{0.9}Sr_{0.1})Mn_{0.8}Co_{0.2}(C_4H_4O_6)_{2.5} \cdot 14H_2O$ ,  $Tb_{0.8}Sr_{0.2}Fe(C_4H_4O_6)_{2.5} \cdot 2H_2O$ , samples indicated a three step decomposition, while  $Gd_{0.6}Sr_{0.4}Ru(C_4H_4O_6)_3 \cdot 4H_2O$ ,  $SrCe_{0.95}Y_{0.05}(C_4H_4O_6)_{2.5} \cdot 3H_2O$  and  $Mn_{0.6}Co_{0.4}Sn(OH)_6$  indicated a two step decomposition at a temperature range of  $25 - 800\text{ }^\circ\text{C}$  respectively. An endothermic peak at around  $100\text{ }^\circ\text{C}$  is attributed to desorption of physically adsorbed water and residual water molecules for these samples respectively. In TGA, the mass loss starts very slowly at  $45\text{ }^\circ\text{C}$  and at around  $180\text{ }^\circ\text{C}$  indicated the removal of water molecules. The dehydrated complex was almost stable upto  $210\text{ }^\circ\text{C}$ . The observed mass loss

and corresponding temperature ranges are shown in Table I. The isothermally heated of these samples under normal air at  $150\text{ }^\circ\text{C}$  respectively, the infrared spectrum showed the absence of the -OH band and a considerable reduction in the intensities of all carboxylate bands.

X-ray diffraction pattern showed polycrystallinity of the samples with decrease in interplanar spacing as compared to the parent compounds. The elemental analysis were in good agreement with the respective anhydrous samples except manganese-cobalt-tin hydroxide, which show the formation of  $Mn_{0.6}Co_{0.4}Sn(OH)_4$  compound. The infrared spectra of this sample showed the presence of OH by the three modes of vibrations at  $3410, 1620$  and  $870\text{ cm}^{-1}$ , which are assigned as stretching, in plane deformation and vibrational lattice mode respectively [45].

After dehydration, there were two strong and broad peak in the DTA curve at approximately  $330\text{ }^\circ\text{C}$  and  $465\text{ }^\circ\text{C}$  for  $(Gd_{0.9}Sr_{0.1})Mn_{0.8}Co_{0.2}(C_4H_4O_6)_{2.5}$  and  $Tb_{0.8}Sr_{0.2}Fe(C_4H_4O_6)_{2.5}$  compounds which reveals to the formation of the final oxide. The TGA showed two-step mass losses in the temperature range of  $180 - 410\text{ }^\circ\text{C}$  and  $410 - 610\text{ }^\circ\text{C}$ , corresponding to the formation of the respective carbonates and final perovskite oxides (see Fig. 1(a) and (b)). The observed mass losses were in reasonable agreement with the calculated values (see Table I).

The infrared spectra of the isothermally heated parent samples at  $380\text{ }^\circ\text{C}$  showed the bands at  $1465\text{ cm}^{-1}$ ,  $1380\text{ cm}^{-1}$  and  $1150\text{ cm}^{-1}$  to carbonate group frequency, along with the weak bands at  $575\text{ cm}^{-1}$  and  $430\text{ cm}^{-1}$  due to M-O stretching frequency, and no band was found at  $1590\text{ cm}^{-1}$  indicating the absence of carboxyl (-COOH) group. The X-ray diffraction pattern of these isothermally heated samples showed generally broad and amorphous nature. The elemental analyses were confirmed with respective carbonate samples. This is also qualitatively test by taking small amount of these solid and adds 2 ml distilled water in a test tube. Then a dropper full of 3M  $H_2SO_4$  trickle down side of test tube. The formation of small bubbles is noted, which indicate carbonate present. The another qualitative test is to prepare a thin film of baryte water ( $Ba(OH)_2$ ) on small platinum wire loop. Then hold near the mouth of test tube which contain above isothermal sample and HCL. The film turns opaque due to  $BaCO_3$ . This is also confirmed carbonate present. The sample thus obtained at  $380\text{ }^\circ\text{C}$  confirmed the presence of respective carbonate. For sample heated isothermally at around  $490\text{ }^\circ\text{C}$ , in the infrared spectra showed two absorption bands in the region  $573\text{ cm}^{-1}$  and  $424\text{ cm}^{-1}$ . These bands may be tentatively assigned to M-O stretching and O-M-O bending vibrations of perovskite phase formation respectively [45]. The spectrum further showed the absence of carbonate group frequency. The X-ray diffraction pattern showed generally sharp lines, and the pattern fit with the respective perovskite oxide [46, 47]. The metal analysis carried out by ICPS analysis agreed well with that of the respective oxides.

The oxidative decomposition of anhydrous precursors such as  $Gd_{0.6}Sr_{0.4}Ru(C_4H_4O_6)_3$  and  $SrCe_{0.95}Y_{0.05}(C_4H_4O_6)_{2.5}$  were indicated by presence of strong and broad exothermic peak on the DTA curve at

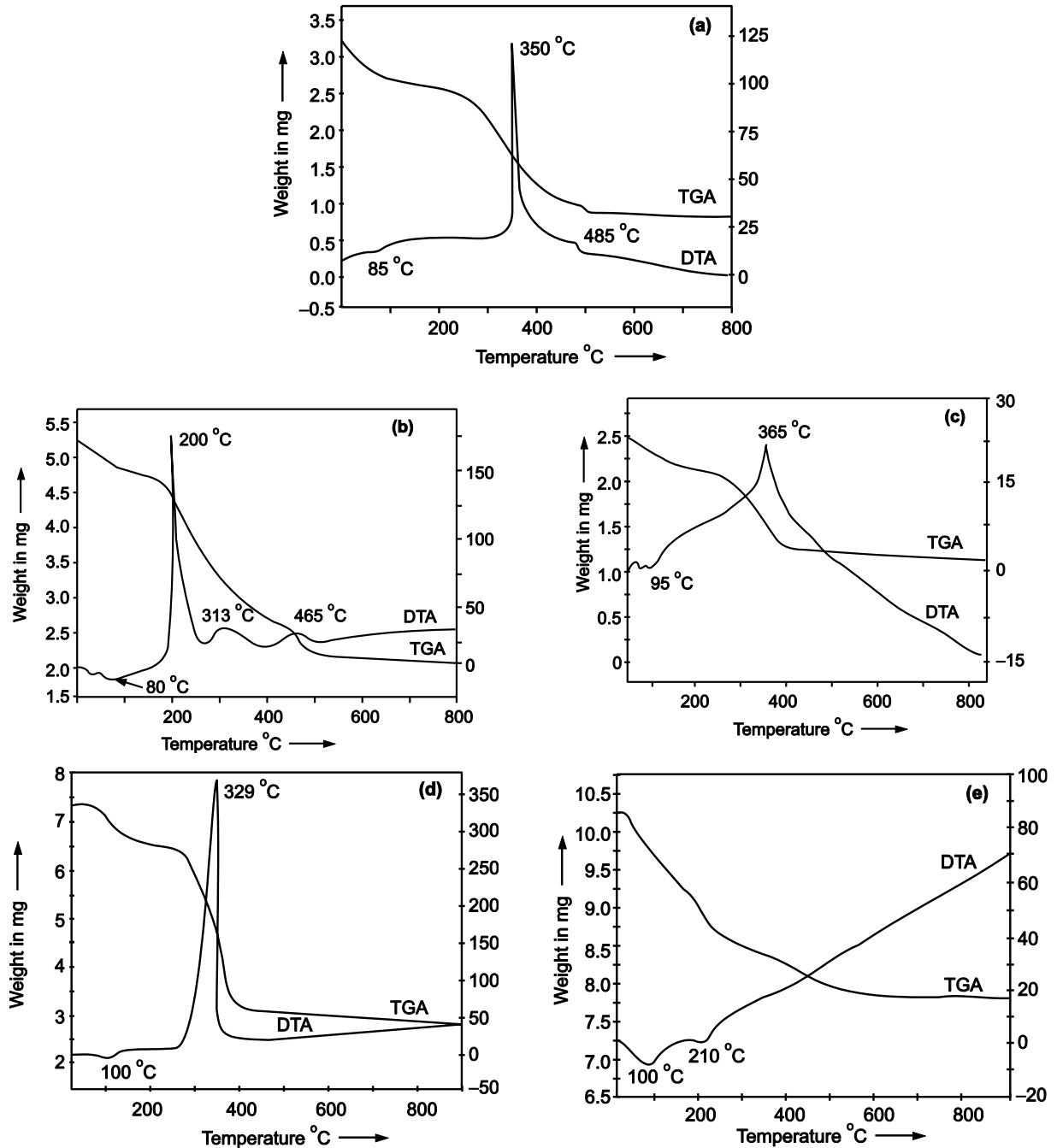


**Fig. 1.** TGA and DTA curves for tartrate / hydroxide precursor in normal air atmosphere.  
 (a)  $(\text{Gd}_{0.9}\text{Sr}_{0.1})\text{Mn}_{0.8}\text{Co}_{0.2}(\text{C}_4\text{H}_4\text{O}_6)_{2.45} \cdot 14\text{H}_2\text{O}$ , (b)  $\text{Tb}_{0.8}\text{Sr}_{0.2}\text{Fe}(\text{C}_4\text{H}_4\text{O}_6)_{2.4} \cdot 2\text{H}_2\text{O}$ , (c)  $\text{Gd}_{0.6}\text{Sr}_{0.4}\text{Ru}(\text{C}_4\text{H}_4\text{O}_6)_{2.8} \cdot 4\text{H}_2\text{O}$ ,  
 (d)  $\text{SrCe}_{0.95}\text{Y}_{0.05}(\text{C}_4\text{H}_4\text{O}_6)_{2.5} \cdot 3\text{H}_2\text{O}$ , (e)  $\text{Mn}_{0.6}\text{Co}_{0.4}\text{Sn}(\text{OH})_6$ .

around 330 °C corresponding in the formation of final oxides. Similarly the decomposition of  $\text{Mn}_{0.6}\text{Co}_{0.4}\text{SnO}(\text{OH})_4$  sample was indicated by an endothermic peak in the DTA curve at 210 °C. The TGA curves for these complexes showed a continuous mass loss from 200 to 600 °C (see Fig. 1 (c), (d) and (e)). These mass losses were found to be in good agreement with the formation of respective perovskite oxide as the final product (see Table I). The X-ray diffraction pattern for the parent samples decomposed isothermally at around 500 °C showed mainly respective perovskite oxide [48-50].

The infrared spectrum of the isothermal product, there are two strong absorption band at about 580  $\text{cm}^{-1}$  and 422  $\text{cm}^{-1}$  (or 650  $\text{cm}^{-1}$  and 552  $\text{cm}^{-1}$  for  $\text{Mn}_{0.6}\text{Co}_{0.4}\text{SnO}_3$  perovskite) which correspond to M-O stretching and O-M-O bending vibration respectively for perovskite oxides [45]. However the infrared spectra of  $\text{Gd}_{0.6}\text{Sr}_{0.4}\text{RuO}_3$  perovskite showed these M-O bands along with a strong band at 2325  $\text{cm}^{-1}$  correspond to carbon dioxide present on the isothermal product. The X-ray diffraction pattern of this sample showed a slightly broad pattern, probably that of adsorbed carbon dioxide on the perovskite (i.e  $\text{Gd}_{0.6}\text{Sr}_{0.4}\text{RuO}_3(\text{CO}_2)$ ). When this

Table I

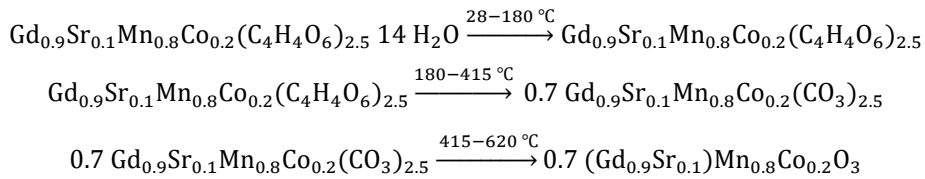
TGA and DTA data of tartrate / hydroxide precursors under static air atmosphere

Precursor	TGA			DTA peak temp. (°C)	Predicted intermediates and final products
	% mass loss		Temp. range (°C)		
	Observed	calculated			
$(\text{Gd}_{0.9}\text{Sr}_{0.1})\text{Mn}_{0.8}\text{Co}_{0.2}(\text{C}_4\text{H}_4\text{O}_6)_{2.5} \cdot 14\text{H}_2\text{O}$	30.30	31.28	30-180	85	$(\text{Gd}_{0.9}\text{Sr}_{0.1})\text{Mn}_{0.8}\text{Co}_{0.2}(\text{C}_4\text{H}_4\text{O}_6)_{2.5}$
	43.48	43.35	180-415	350	$0.7(\text{Gd}_{0.9}\text{Sr}_{0.1})\text{Mn}_{0.8}\text{Co}_{0.2}(\text{CO}_3)_{2.5}$
	28.46	28.46	415-620	485	$0.7(\text{Gd}_{0.9}\text{Sr}_{0.1})\text{Mn}_{0.8}\text{Co}_{0.2}\text{O}_3$
$\text{Tb}_{0.8}\text{Sr}_{0.2}\text{Fe}(\text{C}_4\text{H}_4\text{O}_6)_{2.5} \cdot 2\text{H}_2\text{O}$	6.67	6.88	25-170	80	$\text{Tb}_{0.8}\text{Sr}_{0.2}\text{Fe}(\text{C}_4\text{H}_4\text{O}_6)_{2.5}$
	39.80	39.10	170-410	200 & 313	$\text{Tb}_{0.8}\text{Sr}_{0.2}\text{Fe}(\text{CO}_3)_{2.5}$
	27.80	27.59	410-630	465	$\text{Tb}_{0.8}\text{Sr}_{0.2}\text{FeO}_3$
$\text{Gd}_{0.6}\text{Sr}_{0.4}\text{Ru}(\text{C}_4\text{H}_4\text{O}_6)_3 \cdot 4\text{H}_2\text{O}$	10.00	10.81	28-230	95	$\text{Gd}_{0.6}\text{Sr}_{0.4}\text{Ru}(\text{C}_4\text{H}_4\text{O}_6)_3$
	52.00	52.08	230-600	365	$\text{Gd}_{0.6}\text{Sr}_{0.4}\text{RuO}_3(\text{CO}_2)$
$\text{SrCe}_{0.95}\text{Y}_{0.05}(\text{C}_4\text{H}_4\text{O}_6)_{2.5} \cdot 3\text{H}_2\text{O}$	8.11	8.36	30-230	100	$\text{SrCe}_{0.95}\text{Y}_{0.05}(\text{C}_4\text{H}_4\text{O}_6)_{2.5}$
	54.41	54.55	230-570	329	$\text{SrCe}_{0.95}\text{Y}_{0.05}\text{O}_3$
$\text{Mn}_{0.6}\text{Co}_{0.4}\text{Sn}(\text{OH})_6$	6.34	6.49	30-120	100	$\text{Mn}_{0.6}\text{Co}_{0.4}\text{Sn}(\text{OH})_4$
	13.54	14.81	120-620	210	$\text{Mn}_{0.6}\text{Co}_{0.4}\text{SnO}_3$

sample is heated at 700°C in normal air atmosphere for one hour, Infrared spectrum showed the absence of carbon dioxide band and X-ray diffraction pattern showed sharp line corresponding to pure Gd<sub>0.6</sub>Sr<sub>0.4</sub>RuO<sub>3</sub> [48]. ICPS analysis was also in good agreement with the respective perovskites. The prescribed intermediates obtained in each temperature region under a normal air atmosphere are shown in Table I. The gaseous products obtained by the thermal decomposition of above tartrate and hydroxide precursors under dynamic (pure and dry) Nitrogen atmosphere were analyzed by qualitative gas detection method. Carbon dioxide was detected by precipitation as calcium carbonate from a solution of calcium hydroxide, while carbon monoxide was detected

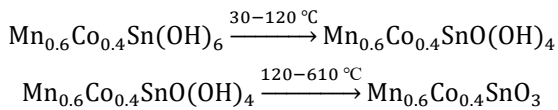
by reduction of iodine pentoxide into iodine. Ethylene gas was detected by the action of bromine water (2 % bromine in CCl<sub>4</sub>), a decolorization of reagent occurs (i.e. due to substitution or addition reactions). Acetylene gas was detected by the action of alcoholic solution on Nessler reagent (i.e. HgCl<sub>3</sub>+KI+NaOH solution called alkaline mercuric iodide reagent), a white or grayish – white precipitate was formed immediately.

Depending upon the results obtained above the following thermal decomposition process in normal air atmosphere may be written as: For Gd<sub>0.9</sub>Sr<sub>0.1</sub>Mn<sub>0.8</sub>Co<sub>0.2</sub>(C<sub>4</sub>H<sub>4</sub>O<sub>6</sub>)<sub>2.5</sub>.14H<sub>2</sub>O precursor may be written as:



A similar thermal decomposition path was also observed for remaining tartrate precursors.

The thermal decomposition of hydroxide precursor i.e. Mn<sub>0.6</sub>Co<sub>0.4</sub>Sn(OH)<sub>6</sub> was observed in the normal air atmosphere.



## 2.2. Characterization of nanosized substituted perovskites

### 2.2.1. Compositional analysis

The substituted perovskites obtained are characterized by metal analysis at the first level, such as (Gd<sub>0.9</sub>Sr<sub>0.1</sub>) Mn<sub>0.8</sub>Co<sub>0.2</sub>O<sub>3</sub>, Tb<sub>0.8</sub>Sr<sub>0.2</sub>FeO<sub>3</sub>, Gd<sub>0.6</sub>Sr<sub>0.4</sub>RuO<sub>3</sub>, SrCe<sub>0.95</sub>Y<sub>0.05</sub>O<sub>3</sub>, and Mn<sub>0.6</sub>Co<sub>0.4</sub>SnO<sub>3</sub>. Recommended analysis methods are used. In Table II, The compositions observed are summarized. They are ± 0.5 % of the nominated value. This finding agrees with the findings of inductively coupled plasma (ICPS). The energy dispersive X-ray analysis (EDS) also demonstrates the existence of the same cationic ratio of all-metal species as originally used (Table II). In the EDS spectrum, the peaks for all the cations were present (Fig. 2). At many places, the elemental composition analysis was uniform, which is representative of a highly homogeneous substance. This is due to the uniform mixing of all the cations. When strontium ions are substituted by rare-earth ions or related ions, the negative effective charges of strontium ions must be compensated for by the creation of equal quantities of positive effective charges. This can either constitute M<sup>4+</sup> ions (e.g. M<sup>4+</sup> can be Mn, Fe, Ru, etc) or vacancies of charged oxygen. EDS and ICPS techniques have calculated the concentration of these ions (see Table II).

### 2.2.2. Structural studies

Structural analysis is made by X-ray diffraction

(XRD) on the substituted perovskites and the diffractograms were obtained from a Siemens D500 diffractometer using CuKα radiation at 2 °/min scanning rate in the 2θ range of 20-80°. The XRD pattern acquired for substituted perovskite such as (Gd<sub>0.9</sub>Sr<sub>0.1</sub>) Mn<sub>0.8</sub>Co<sub>0.2</sub>O<sub>3</sub>, Tb<sub>0.8</sub>Sr<sub>0.2</sub>Fe<sub>2</sub>O<sub>3</sub>, Gd<sub>0.6</sub>Sr<sub>0.4</sub>RuO<sub>3</sub>, SrCe<sub>0.95</sub>Y<sub>0.05</sub>O<sub>3</sub> and Mn<sub>0.6</sub>Co<sub>0.4</sub>SnO<sub>3</sub> are shown in Fig.3. There is an excellent agreement of experimental XRD pattern with the standard JCPDS pattern confirming the monophasic perovskite structure of these substituted oxides [46-50]. The X-ray diffraction peaks are found to be broad and it is attributed to the nanocrystalline nature of these perovskites. The peaks for these substituted perovskite appear approximately at same position as for the respective unsubstituted perovskites but with different intensities. In these cases, the substituent ions seem to dissolve / arrange in the perovskite structure to fulfill the formation of single perovskite phase. The hkl values are assigned to the peaks in the XRD are shown in Fig. 3. The lattice parameter for these substituted compounds are determined from the XRD pattern using the inter-plane spacing d of the diffraction peak and hkl denotes the miller indices of the corresponding peak in the orthorhombic or cubic relation. The correct structured orthorhombic perovskite except for the Tb<sub>0.8</sub>Sr<sub>0.2</sub>Fe<sub>2</sub>O<sub>3</sub> and Mn<sub>0.6</sub>Co<sub>0.4</sub>SnO<sub>3</sub> compounds, which is found to be a cubic and rhombohedral structure respectively, was revealed by all substituted compounds. The d-spacing and relative intensity values observed experimentally are compared with those recorded in the literature [46-50]. The lattice parameters, unit cell volume, average cation sizes of A – site perovskite < R<sub>A</sub> >, and mismatch factor (σ<sup>2</sup>) for each compound are listed in Table III. It is shown that for all samples, the observed lattice parameters and unit cell volume are substantially decreased compared to the reported unsubstituted perovskites. (see Table III) [46-50]. In agreement with the lanthanide contraction, the unit cell decreases. The bond distance between elements decreases when an electron is added to the 4f orbital of rare-earth (RE) elements. Therefore the

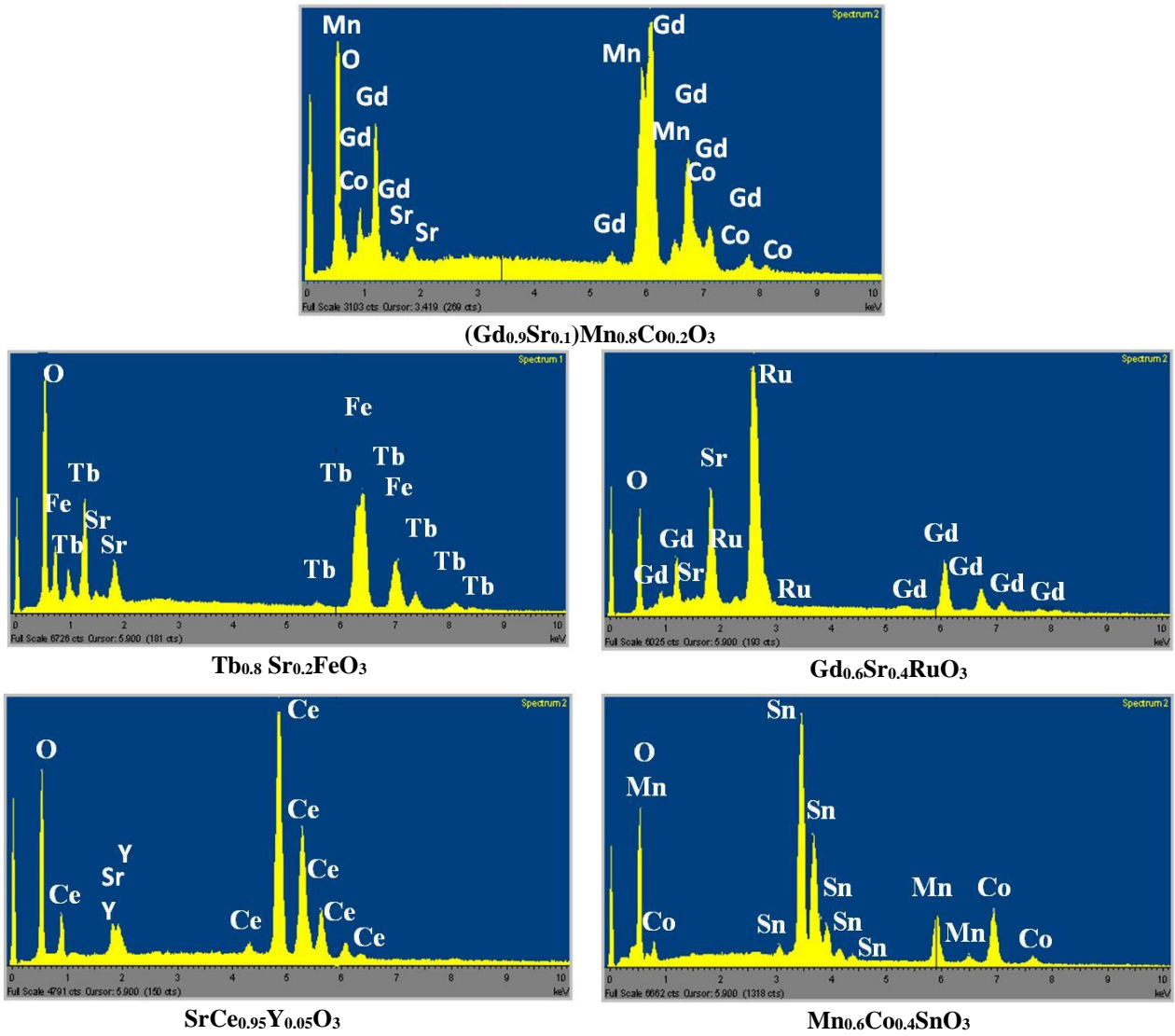


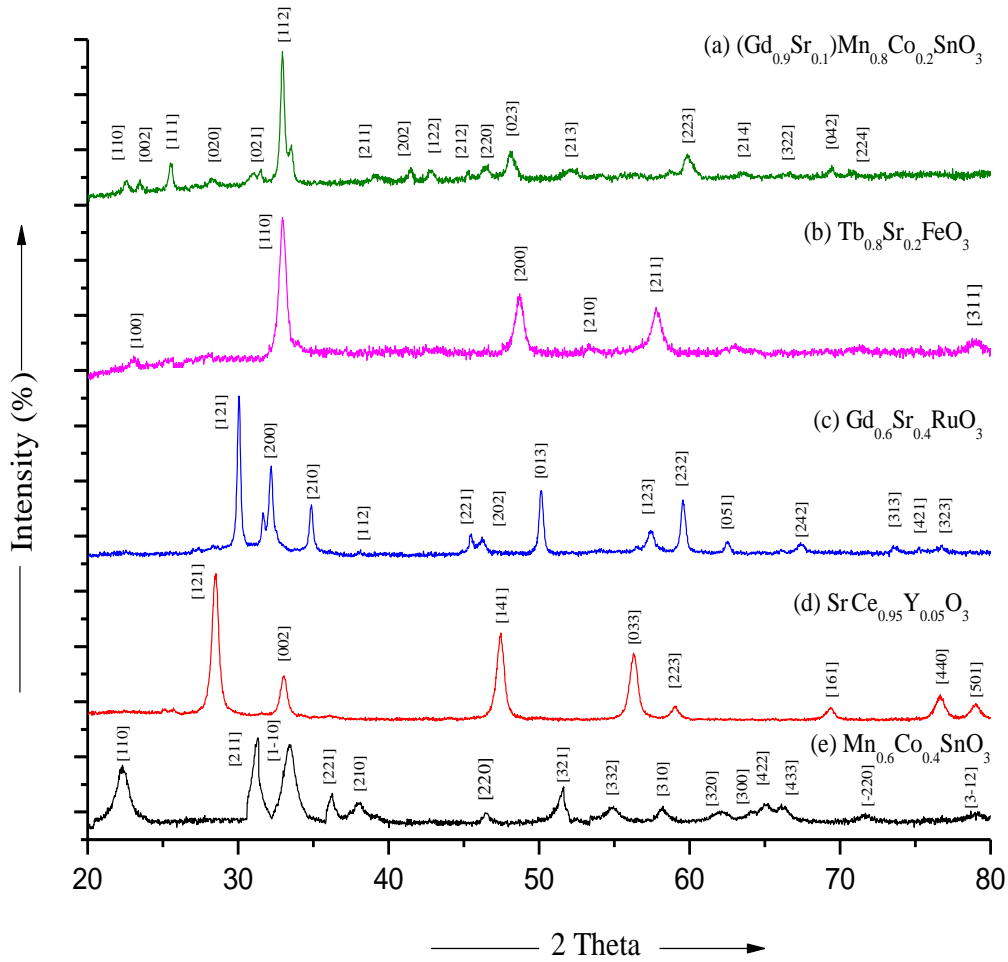
Fig. 2. Energy dispersive X-ray analysis (EDS) of nanosized substituted perovskite compounds.

Table II

Observed ICPES and EDS analysis of nanosized substituted perovskite compounds

Prcursor	Elemental analysis in wt % ( $\pm 0.5$ )							
	Req	Found	Req	Found	Req	Found	Req	Found
$(\text{Gd}_{0.9}\text{Sr}_{0.1})\text{Mn}_{0.8}\text{Co}_{0.2}\text{O}_3$	Gd		Sr		Mn		Co	
	55.71	54.96 (55.07)*	3.45	3.32 (3.66)	17.30	16.96 (17.65)	4.64	4.20 (4.54)
$\text{Tb}_{0.8}\text{Sr}_{0.2}\text{FeO}_3$	Tb		Sr		Fe		--	
	51.16	52.03 (51.82)	7.05	6.81 (6.96)	22.47	21.86 (22.76)	--	--
$\text{Gd}_{0.6}\text{Sr}_{0.4}\text{RuO}_3$	Gd		Sr		Ru		--	
	33.88	34.23 (33.71)	12.59	13.03 (13.22)	36.30	36.39 (36.13)	--	--
$\text{SrCe}_{0.95}\text{Y}_{0.05}\text{O}_3$	Sr		Ce		Y		--	
	32.07	32.46 (32.77)	48.73	49.01 (48.41)	1.63	1.54 (1.74)	--	--
$\text{Mn}_{0.6}\text{Co}_{0.4}\text{SnO}_3$	Mn		Co		Sn		--	
	14.76	15.06 (14.91)	10.56	10.28 (10.72)	53.18	53.38 (53.63)	--	--

\*The figures in parenthesis indicate metal analysis obtained from EDS method



**Fig. 3.** X-ray diffraction patterns of nanosized substituted perovskite compounds.

(a)  $(\text{Gd}_{0.9}\text{Sr}_{0.1})\text{Mn}_{0.8}\text{Co}_{0.2}\text{O}_3$ , (b)  $\text{Tb}_{0.8}\text{Sr}_{0.2}\text{FeO}_3$ , (c)  $\text{Gd}_{0.6}\text{Sr}_{0.4}\text{RuO}_3$ , (d)  $\text{SrCe}_{0.95}\text{Y}_{0.05}\text{O}_3$ , (e)  $\text{Mn}_{0.6}\text{Co}_{0.4}\text{SnO}_3$ .

**Table III**

Structural data of nanosized substituted perovskite compounds

Compounds	structure	X-ray analysis (nm)			Unit cell volume (nm) <sup>3</sup>	Average cation sizes of A site of perovskite <math>\langle R_A \rangle \text{\AA}</math>	Mismatch factor $\sigma^2$ ( $\text{\AA})^2$	Tolerance factor (t)
		Lattice parameter						
		a	b	c				
$(\text{Gd}_{0.9}\text{Sr}_{0.1})\text{Mn}_{0.8}\text{Co}_{0.2}\text{O}_3$	Orthorhombic	0.522 (0.531)*	0.576 (0.584)	0.737 (0.743)	0.222 (0.230)	1.109	$4.7610 \times 10^{-5}$	0.8993
$\text{Tb}_{0.8}\text{Sr}_{0.2}\text{FeO}_3$	cubic	0.381 (0.386)	-	-	0.055 (0.057)	1.102	$1.96 \times 10^{-4}$	0.9072
$\text{Gd}_{0.6}\text{Sr}_{0.4}\text{RuO}_3$	Orthorhombic	0.549 (0.553)	0.762 (0.785)	0.545 (0.557)	0.228 (0.242)	1.116	$1.2696 \times 10^{-4}$	0.8554
$\text{SrCe}_{0.95}\text{Y}_{0.05}\text{O}_3$	Orthorhombic	0.605 (0.613)	0.847 (0.858)	0.596 (0.599)	0.305 (0.315)	1.13	-	0.6907
$\text{Mn}_{0.6}\text{Co}_{0.4}\text{SnO}_3$	Rhombohedral	0.564 (0.574)	0.564 (0.574)	0.564 (0.574)	0.114 (0.120)	0.559	$2.94 \times 10^{-4}$	0.7104

\*The figures in parenthesis are lattice parameter of reported unsubstituted perovskites [46-50]

distance between RE-O bonds is shorter than the critical distance. The unit cell shrinkage at the B-site does not

occur from a decrease in M-O bond distances (M = transition metals) but a bending of the M-O-M bond

angle away from 180°.

The size of the cation on the A-site affects the crystal symmetry significantly in perovskite (ABO<sub>3</sub>), while that of the cation on the B-site does not change the symmetry, but proportionally changes the volume of the lattice (i.e. unit cell volume). Rodrigues and Attfield [51] argued that local distortions and stresses in the structure were caused by size differences between different A-site ions. In terms of the variance of the distribution of cation radii,  $\sigma^2 = \sum \{xR_A^2 - \langle R_A \rangle^2\}$ , a quantitative explanation of this effect was given. Here at the A-site species of the perovskite,  $x$  is the fractional occupancies for different cations,  $R_A$  their ionic radii, while  $\langle R_A \rangle$  is the average cation size. The effects of the mismatch factor ( $\sigma^2$ ) have been determined for the various cations of substituted perovskite compounds and are shown in Table III. Standard ionic radii [52-53] i.e. Gd<sup>3+</sup> (1.107 Å), Sr<sup>2+</sup> (1.310 Å), Tb<sup>3+</sup> (1.095 Å), Ce<sup>3+</sup> (1.196 Å), Y<sup>3+</sup> (1.075 Å), Mn<sup>3+</sup> (0.580 Å), Co<sup>3+</sup> (0.545 Å), Fe<sup>3+</sup> (0.550 Å), Ru<sup>3+</sup> (0.681 Å) and Sn<sup>4+</sup> (0.55 Å) were used for the calculation of  $\langle R_A \rangle$  mean cation sizes and 8-coordination mismatch factor ( $\sigma^2$ ) for orthorhombic or cubic perovskites. The average cation size of cations at the A-site of perovskite  $\langle R_A \rangle$  is less than 1.21 Å, as is evident from Table III, suggesting the absence of long-range cooperative Jahn-Teller distortion in the compounds [54]. However, the probability of dynamic Jahn-Teller short-length distortion cannot be eliminated [55].

The additional disorder is caused by the substitution of a small amount of Sr<sup>2+</sup> ion and can occur between the A-site cations due to the size mismatch factor ( $\sigma^2$ ) [51]. We have observed that the mismatch factor ( $\sigma^2$ ) varies with compounds (Table III). This is due to segregation of the A-site cations, as a result of the large size disparities, so that the compounds are no longer microscopically homogeneous, although they appear to be concluded, provided the constant A-site cation average radius  $\langle R_A \rangle = 1.21$  Å, the variation of the A-site disorder as characterized by variance  $\sigma^2$  causes no change of the crystal structure. In addition to these effects, the strain field associated with local oxygen ion displacement is likely to become so small that no chemical phase separation occurs in the system. Oxygen stoichiometry was calculated by iodometric titration for all substituted substances, the error in the determination being  $\pm 0.2$ . It was found that all the compounds in the 2.98 to 3.00 range had the same amount of oxygen. This means that the stoichiometry of oxygen in these compounds is retained perfectly. Using the relationship [56]  $Q = \sqrt{2} (\langle R_A^2 \rangle - \langle R_A \rangle^2)$ , the local oxygen displacement  $Q$  was determined. The  $Q$  values are observed in the range 0.000067 to 0.000416. It concludes that in all substituted compounds, a negligible amount of oxygen displacement occurs. Tolerance factors for these compounds were determined using the relationship  $t = [\langle R_A \rangle + R(O)] / \sqrt{2} [\langle R_B \rangle + R(O)]$ , where  $t$  = tolerance factors,  $R(O) = 1.40$  Å is the ionic size of the O<sup>2-</sup>, (for six coordinated radii),  $\langle R_A \rangle$  and  $\langle R_B \rangle$  are the mean ionic sizes of the A and B-site ions, respectively, for the perovskite structure, respectively [52, 53]. Tolerance factors ( $t$ ) are shown in Table III. The tolerance factors ranged from 0.6907 to 0.9072, well within the 0.68 - 1.00 range which characterizes the stable perovskite

structures.

We calculate the particulate properties such as mean crystallite size  $\langle D \rangle_{X\text{-ray}}$ , density ( $D_x$ ), apparent density ( $D$ ), and porosity ( $P$ ) for all substituted compounds are summarized in Table IV. As can be seen from the table, the crystallite sizes  $\langle D \rangle_{X\text{-ray}}$  are in the range between 14.85 nm to 47.72 nm. The apparent density ( $D$ ) observed is lower than the X-ray density ( $D_x$ ). This low density indicates the formation of a microstructure with a smaller average grain size.

For all substituted perovskite samples, the morphology of the particles produced was examined by scanning electron micrographs (SEM) (Fig. 4). The grain shape of (Gd<sub>0.9</sub>Sr<sub>0.1</sub>)Mn<sub>0.8</sub>Co<sub>0.2</sub>O<sub>3</sub> is spherical, but with less degree of agglomeration. In comparison to this, the grains of Tb<sub>0.8</sub>Sr<sub>0.2</sub>FeO<sub>3</sub> and SrCe<sub>0.95</sub>Y<sub>0.05</sub>O<sub>3</sub> have a high degree of agglomeration with spherical samples. The grains of Gd<sub>0.6</sub>Sr<sub>0.4</sub>RuO<sub>3</sub> were plate-like and no agglomerated, while the grains of Mn<sub>0.6</sub>Co<sub>0.4</sub>SnO<sub>3</sub> had needle-like less agglomerated; but some needle grains have already been destroyed.

Fig. 5 displays the TEM images of substituted perovskites. As can be seen for (Gd<sub>0.9</sub>Sr<sub>0.1</sub>)Mn<sub>0.8</sub>Co<sub>0.2</sub>O<sub>3</sub>, Tb<sub>0.8</sub>Sr<sub>0.2</sub>FeO<sub>3</sub> and SrCe<sub>0.95</sub>Y<sub>0.05</sub>O<sub>3</sub>, (Fig.5 (a)), (b), (d)), the particles are more or less spherical with a size range between 22 nm to 77 nm for these samples. Square particles were present in the TEM picture of the Gd<sub>0.6</sub>Sr<sub>0.4</sub>RuO<sub>3</sub> sample (Fig. 5(c)); in contrast to this, the particles Mn<sub>0.6</sub>Co<sub>0.4</sub>SnO<sub>3</sub> (Fig. 5 (e)) had needle shape particles. Because it corresponds to the inner shell (ordered) region of the particles, without the severely distorted peripheral part, the mean crystallite size determined by XRD is typically smaller than the average particle size determined by TEM. The transmission electron microscopy is a local technique and determines the size of the particles in a limited field of view particle size determination from dynamic light scattering data is highly dependent on the powder dispersion process in glycerol, intended to deagglomerate the nanoparticles. Mechanical mixing, however, breaks down not all agglomerates, so the measured average particle size usually exceeds the XRD mean crystallite size.

Structural information from the selected field of electron diffraction (SAED) was also collected for all samples shown in Fig. 5. It is apparent that all the lattice planes are clearly distinct, suggesting that there is no defect in the single crystalline particle. In the SAED pattern, the various lattice planes are allocated and these are in good agreement with the crystallographic phase of the substituted perovskite system.

An infrared spectrum of a molecule is considered to be unique physical property and is characteristic of the molecule. The infrared spectrum for all substituted perovskite consists of two absorption bands associated with the stretching and bending vibration in the region 400 - 900 cm<sup>-1</sup>. The stretching vibration is assigned to an absorption band in each range at the higher frequency  $\nu_1 = 542$  cm<sup>-1</sup> and the bending vibration at the lower frequency  $\nu_2 = 442$  cm<sup>-1</sup> (Table IV). This is due to the change in the potential energy in the two natural vibrations due to repulsive forces between metal ions and oxygen ions.

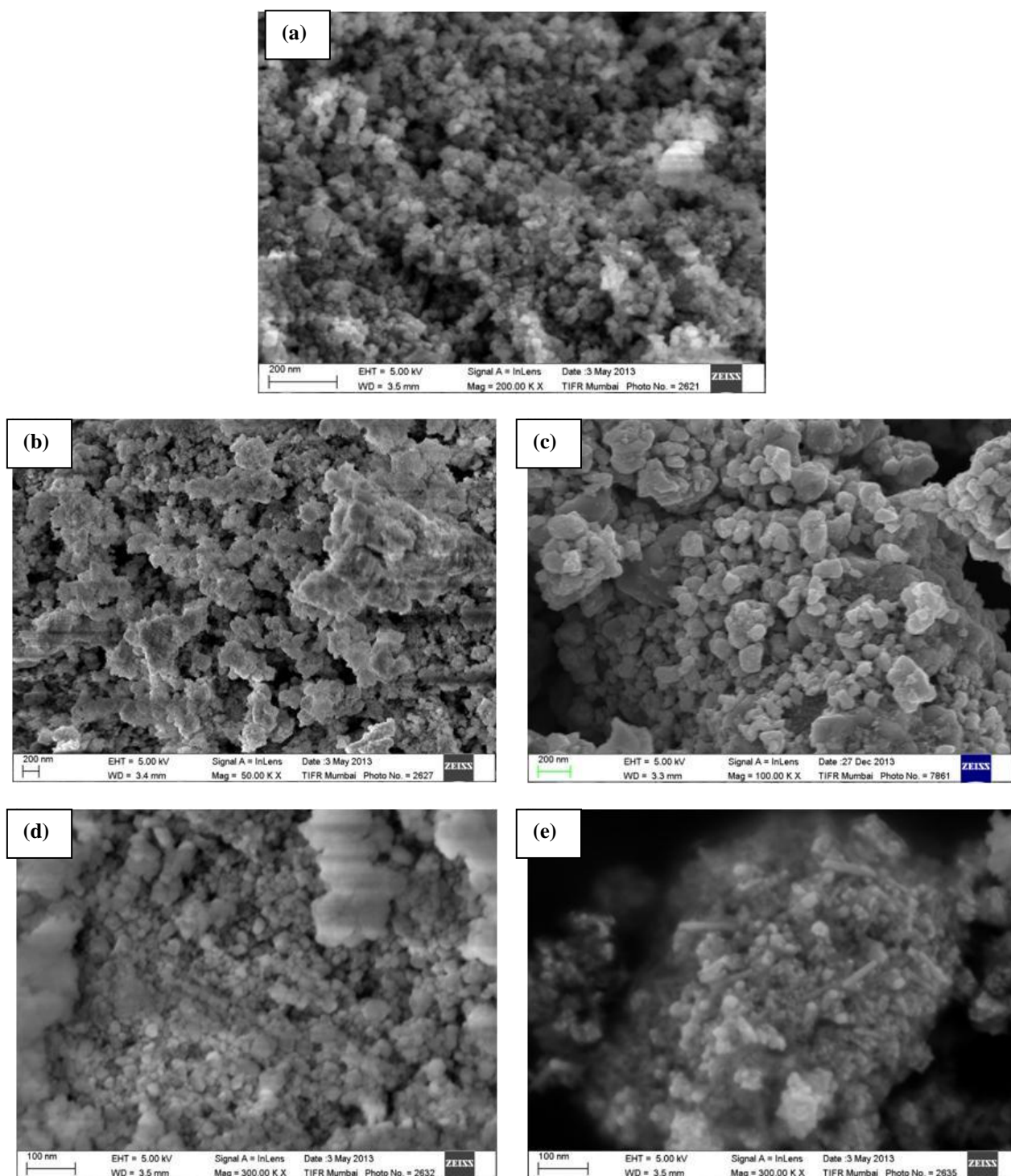


**Fig.4.** Scanning electron micrographs (SEM) of nanosized substituted perovskite compounds. (a)  $Gd_{0.9}Sr_{0.1}Mn_{0.8}Co_{0.2}O_3$ , (b)  $Tb_{0.8}Sr_{0.2}FeO_3$ , (c)  $Gd_{0.6}Sr_{0.4}RuO_3$ , (d)  $SrCe_{0.95}Y_{0.05}O_3$ , (e)  $Mn_{0.6}Co_{0.4}SnO_3$ .

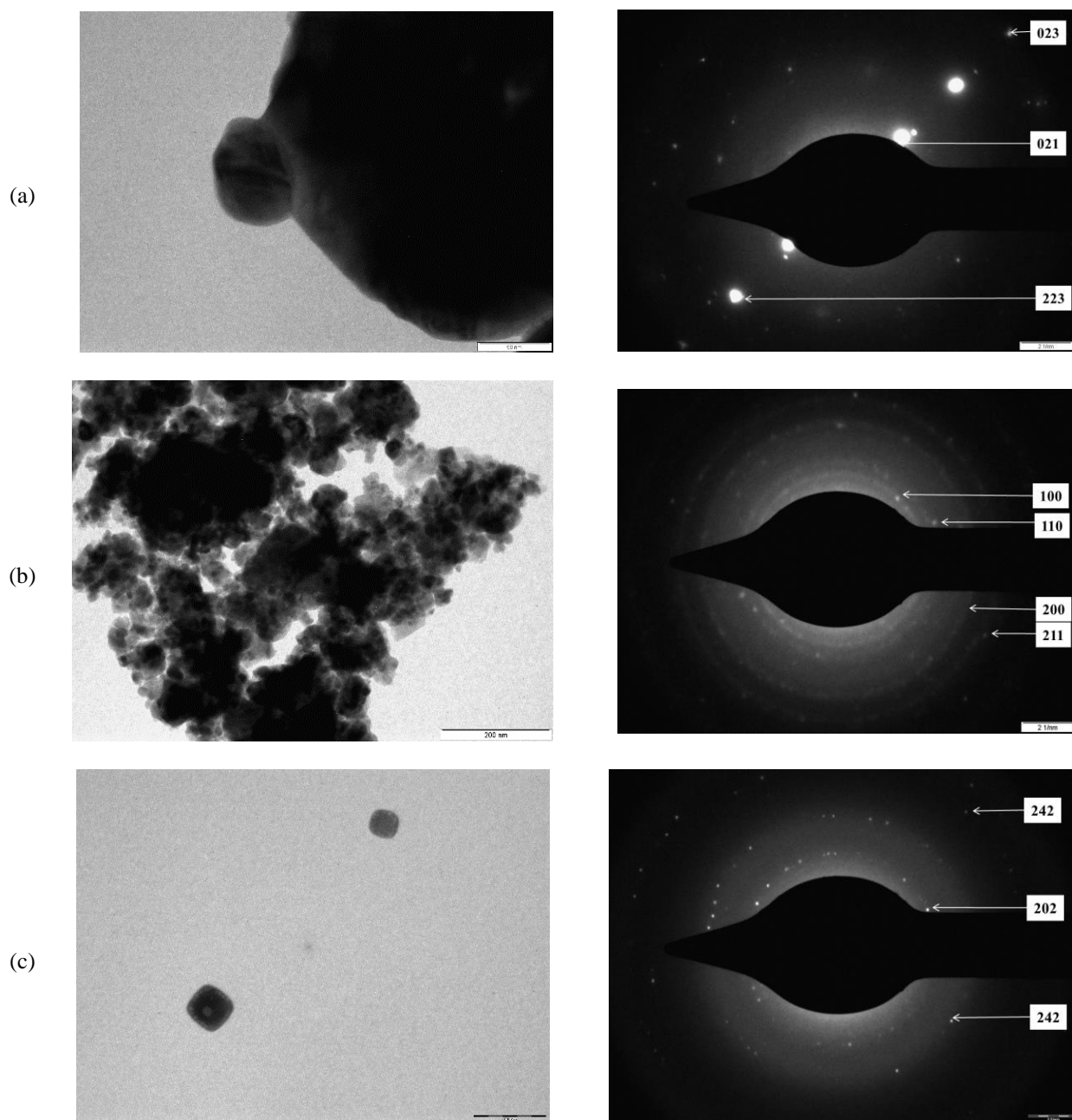
**Table IV**

Particulate properties and infrared spectral data for nanosized substituted perovskite compounds

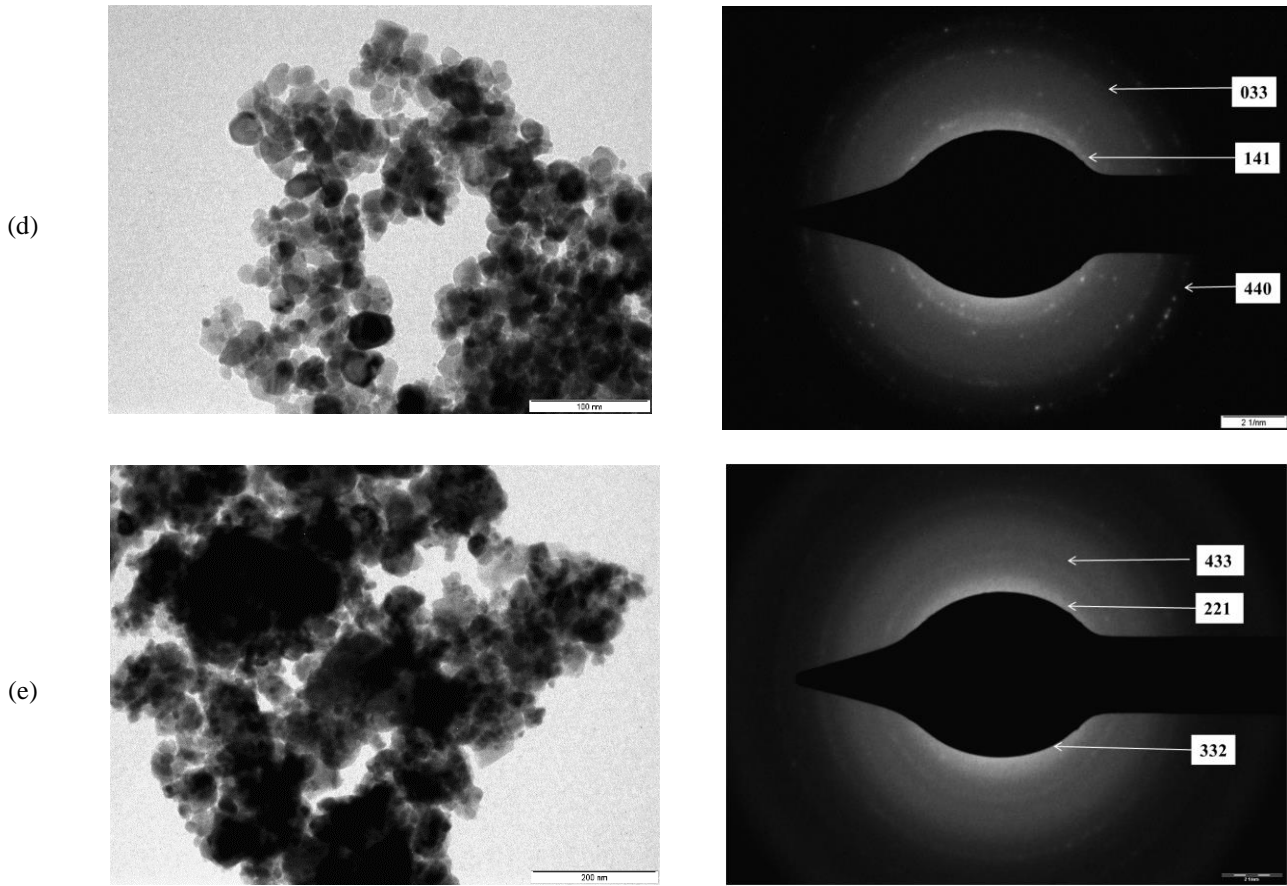
Compounds	Mean crystallite size $\langle D \rangle_{X\text{-Ray}}$ nm $\pm 10\%$	X-Ray density $D_x$ ( $g \cdot cm^{-3}$ )	Apparent density D ( $g \cdot cm^{-3}$ )	Porosity $P=1-D/D_x$	Average particle size (from SEM) nm	Average particle size (from TEM) nm	Infrared spectral absorption band $cm^{-1}$	
							$\nu_1$	$\nu_2$
$(Gd_{0.9}Sr_{0.1})Mn_{0.8}Co_{0.2}O_3$	38.52	7.17	2.425	0.662	50	56	542	442

Table IV (continuation)

$Tb_{0.8}Sr_{0.2}FeO_3$	21.55	4.60	1.566	0.659	15	29	543	425
$Gd_{0.6}Sr_{0.4}RuO_3$	47.72	7.37	1.742	0.764	67	77	524	414
$SrCe_{0.95}Y_{0.05}O_3$	19.86	5.69	2.573	0.548	21	26	568	482
$Mn_{0.6}Co_{0.4}SnO_3$	14.85	2.07	1.615	0.22	17	22	635	483



**Fig.5.** Transmission electron micrographs (TEM) and SAED pattern of nanosized substituted perovskite compounds. (a)  $(Gd_{0.9}Sr_{0.1})Mn_{0.8}Co_{0.2}O_3$ , (b)  $Tb_{0.8}Sr_{0.2}FeO_3$ , (c)  $Gd_{0.6}Sr_{0.4}RuO_3$ ,



**Fig.5.** Transmission electron micrographs (TEM) and SAED pattern of nanosized substituted perovskite compounds. (d)  $\text{SrCe}_{0.95}\text{Y}_{0.05}\text{O}_3$ , (e)  $\text{Mn}_{0.6}\text{Co}_{0.4}\text{SnO}_3$ .

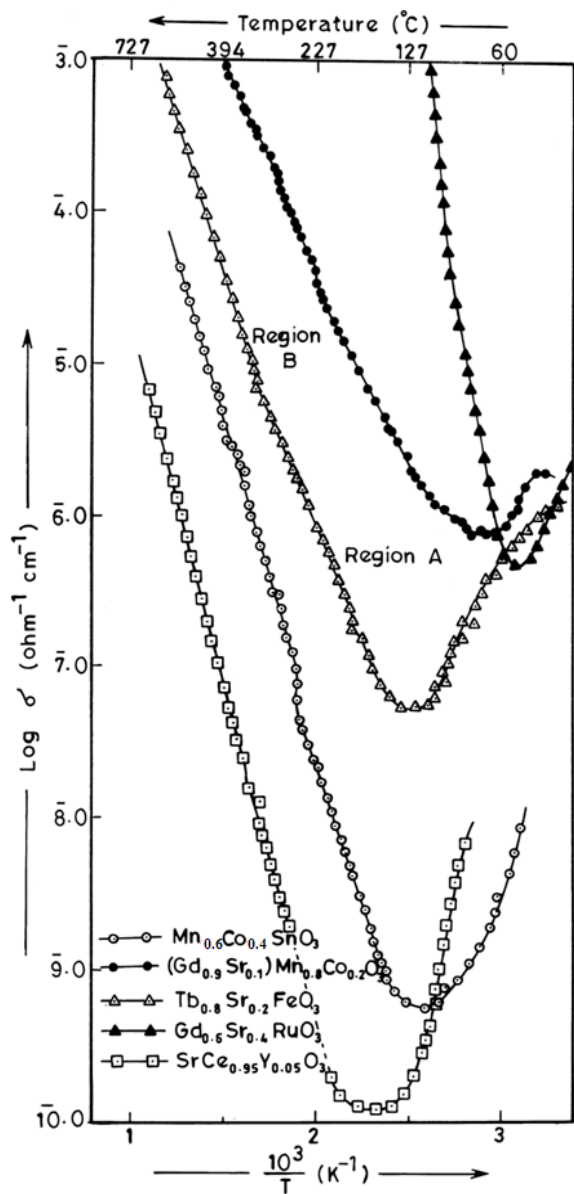
### 2.2.3. Electrical conductivity studies

Fig. 6 indicates the dependence of  $\log \sigma$  against the reciprocal temperature ( $T^{-1}$ ) for  $(\text{Gd}_{0.9}\text{Sr}_{0.1})\text{Mn}_{0.8}\text{Co}_{0.2}\text{O}_3$ ,  $\text{Tb}_{0.8}\text{Sr}_{0.2}\text{FeO}_3$ ,  $\text{Gd}_{0.6}\text{Sr}_{0.4}\text{RuO}_3$ ,  $\text{SrCe}_{0.95}\text{Y}_{0.05}\text{O}_3$  and  $\text{Mn}_{0.6}\text{Co}_{0.4}\text{SnO}_3$  compounds. With increasing temperature, the conductivity increases linearly. At a certain temperature,  $T_c$  indicates a break in the line of each compound, resulting in a change in the slope. The slope shift is typically supposed to occur at the Curie temperature or due to the presence of two parallel mechanisms of conductivity mechanism with different activation energies [57]. For all compounds, the activation energy  $E_a$  (eV) was determined from the slopes of the line before and after transition point  $T_c$  and is tabulated in Table V. The values of activation energies imply that the conduction is due to the process of polarons hopping mechanism. In Region A the value of  $E_a$  is found to be lower than in Region B. The conduction of impurity is favored below 500 K, thus hopping of polarons at higher temperatures. The sample of  $\text{Gd}_{0.6}\text{Sr}_{0.4}\text{RuO}_3$  ( $\text{Ru}^{3+}$  has a  $4d^5$  configuration) showed semiconducting rather than metallic properties. The electrical conduction would then become an activated process, via transfer of an electron from  $t_{2g}$  ( $\Pi^*$ ) to  $e_g$  ( $\sigma^*$ ) levels, which would presumably also exist as band states i.e  $\sigma$ -bonding being stronger than  $\Pi$  bonding. Therefore the electrical behavior in these samples under

investigation is due to the electron acceptor hopping in the sublattice between  $\text{Mn}^{3+} \leftrightarrow \text{Mn}^{4+}$  or  $\text{Ru}^{3+} \leftrightarrow \text{Ru}^{4+}$  or  $\text{Ce}^{3+} \leftrightarrow \text{Ce}^{4+}$  ions of the respectively substituted perovskite under investigation results in increased activation energy ( $E_a$ ) in the region B. The A-site cation disorder has previously been shown to decrease the break temperature,  $T_c$  [58]. In all substituted perovskite compounds, it seems that the A-site cation mismatch factor ( $\sigma^2$ ) tends to play a more important role than the average cation sizes  $\langle R_A \rangle$ .

The significantly different transport behavior on various mismatch factor values ( $\sigma^2$ ) enables us to argue the essential role of A-site disorder in mediating the phase separation of B-site cations, nothing that no charge order phase appears upon the A-site disordered. In other words, the addition of a different substituent can be affected by many factors like the nature of the substituent, the amount of substituent incorporated creating structural defects, and changing its microstructure. Therefore, we turn to the magnetic behavior of these compounds in order to reveal the magnetic ground state in the B-site cations of different A-site disorder degrees.

The temperature effect of all substituted perovskites on the thermoelectric power is shown in Fig. 7. Positive charge carriers for samples of  $(\text{Gd}_{0.9}\text{Sr}_{0.1})\text{Mn}_{0.8}\text{Co}_{0.2}\text{O}_3$  and  $\text{SrCe}_{0.95}\text{Y}_{0.05}\text{O}_3$  decrease slowly with temperatures of



**Fig. 6.** Plot of  $\log \sigma$  against  $T^{-1}$  of nanosized substituted perovskite compounds.

up to 500 K and then almost constant as temperatures rise. In the entire temperature range, the positive values of the thermoelectric power confirmed the p-type semi conduction. Therefore the number of  $Mn^{3+}$  or  $Ce^{3+}$  ions at the B-site of these compounds is greater than the number of  $Mn^{4+}$  or  $Ce^{4+}$  ions at temperatures up to 500 K. As electron transform from  $Mn^{3+} \rightarrow Mn^{4+}$  or  $Ce^{3+} \rightarrow Ce^{4+}$ . The motion of  $Mn^{4+}$  or  $Ce^{4+}$  ions in the lattice of  $Mn^{3+}$  or  $Ce^{3+}$  ions can be visualized as the motion of a hole.

The thermoelectric power of  $Tb_{0.8}Sr_{0.2}FeO_3$  and  $Mn_{0.6}Co_{0.4}SnO_3$  compounds, on the other hand, showed that they were n-type semiconductors. This change in semiconductivity in the perovskite structure depends on the existence of both the A-site cation and B-cation. In general, (i) greater A-site cation causes greater reduction stability. Which is n-type of semiconductor. These findings suggest that the substituent is an electron donor in the conduction band also creates more vacancies. Here, oxygen vacancies act as donor's centers. (ii)

Secondly, rare-earth ions (such as  $Gd^{3+}$ ,  $Tb^{3+}$ ) are

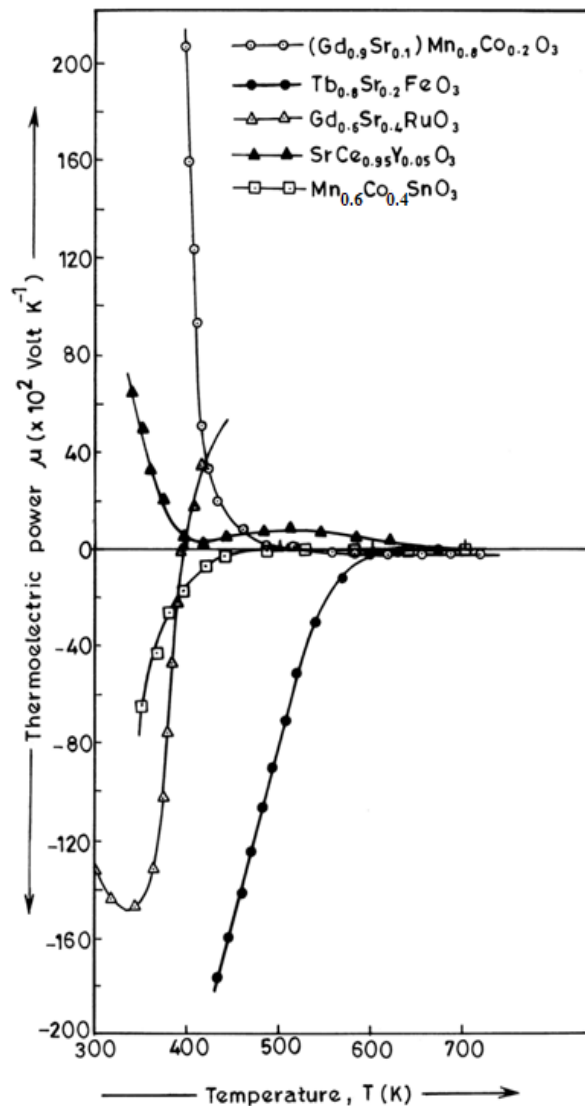


**Fig. 7.** Plot of thermoelectric power,  $\mu$  (volt  $K^{-1}$ ) against temperature,  $T$  (K) of nanosized substituted perovskite compounds.

becoming more acidic. It competes more strongly with the B-site for binding to oxygen atoms of the perovskite. (iii) Stannate have a continuous edge-sharing of transition metal ions (i.e.  $Mn^{2+}$  and  $Co^{2+}$ ) and  $Sn^{4+}$  octahedra is a necessary criterion for the formation of semi-metallic conductivity [59].

Similarly, n-type semiconductivity is demonstrated by the  $Gd_{0.6}Sr_{0.4}RuO_3$  compound. This could happen only charge carriers are localized on the defect centers, which are inherently present in the solids. The  $Ru^{4+}$  ion obviously traps carriers. In which, the electron hopping from site to site within the 4d band of ruthenium and secondly, the reduction by Ru-O distance and Ru-O-Ru angle, which corresponds to the electron hopping from  $Ru^{4+}$  to  $Ru^{3+}$  ions, respectively.

We have measured the Hall effect constant in the 0.54 T magnetic field at room temperature after passing current in nA through samples.

Table V

Electrical conductivity data and dielectric properties of nanosized substituted perovskite compounds

Compounds	Temperature corresponding to desorption of adsorbed water (K)	Conductivity measurements				Hall effect measurements at room temperature					
		Region	Temp.range (k)	Activation energy Ea (ev)	Break temp. (transition temperature) T <sub>c</sub> (k)	Current passed (nA)	Resistivity at room temp. Ohm cm	Types of charge carriers	Average Hall coefficient cm <sup>3</sup> /C	Mobility cm <sup>2</sup> /Vs	
(Gd <sub>0.9</sub> Sr <sub>0.1</sub> ) Mn <sub>0.8</sub> Co <sub>0.2</sub> O <sub>3</sub>	348	A	303-500	0.455	500	10	3.705x10 <sup>10</sup>	n-Type	-	8.134x10 <sup>9</sup>	0.22
		B	500-805	0.556							
Tb <sub>0.8</sub> Sr <sub>0.2</sub> FeO <sub>3</sub>	399	A	303-553	0.609	553	15	3.133x10 <sup>7</sup>	n-Type	-	4.408x10 <sup>10</sup>	1407.00
		B	553-805	0.755							
Gd <sub>0.6</sub> Sr <sub>0.4</sub> RuO <sub>3</sub>	370	-	303-805	0.538	-	15	5.577x10 <sup>7</sup>	n-Type	-	9.056x10 <sup>9</sup>	162.40
SrCe <sub>0.95</sub> Y <sub>0.05</sub> O <sub>3</sub>	416	A	303-610	0.841	610	20	8.750x10 <sup>7</sup>	P-Type	-	1.796x10 <sup>9</sup>	20.52
		B	610-805	0.945							
Mn <sub>0.6</sub> Co <sub>0.4</sub> SnO <sub>3</sub>	398	A	303-525	0.683	525	50	4.199x10 <sup>6</sup>	n-Type	-	9.239x10 <sup>8</sup>	220.00
		B	525-805	0.830							

Table V reveals that (Gd<sub>0.9</sub>Sr<sub>0.1</sub>) Mn<sub>0.8</sub>Co<sub>0.2</sub>O<sub>3</sub>, Tb<sub>0.8</sub>Sr<sub>0.2</sub>FeO<sub>3</sub>, Gd<sub>0.6</sub>Sr<sub>0.4</sub>RuO<sub>3</sub>, Mn<sub>0.6</sub>Co<sub>0.4</sub>SnO<sub>3</sub> are n-type semiconductors due to electron hopping between A site cations, while SrCe<sub>0.95</sub>Y<sub>0.05</sub>O<sub>3</sub> suggests p-type semiconductors due to hole hopping between B site cations. The specific resistivity values were observed for all compounds around 4.199 x 10<sup>6</sup> to 3.705 x 10<sup>10</sup> ohm.cm at current passed ranging from 10 to 50 nA. The variations in the observed specific resistivities were also reflected in the mobility. The Hall coefficient at room temperature for all compounds under investigation is negative except the SrCe<sub>0.95</sub>Y<sub>0.05</sub>O<sub>3</sub> compound indicating electrons are the majority carrier. The SrCe<sub>0.95</sub>Y<sub>0.05</sub>O<sub>3</sub> shows p-type conductivity. The variations of the observed Hall coefficient are also reflected in mobility.

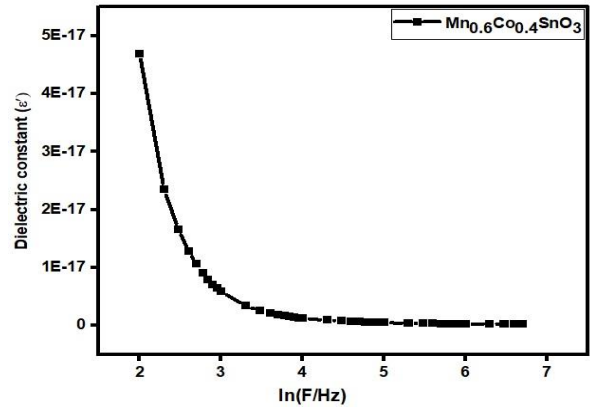
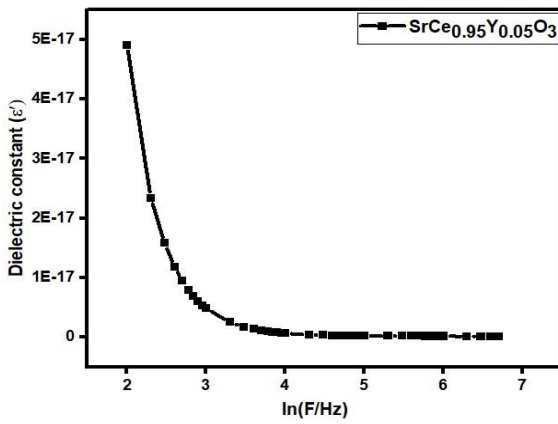
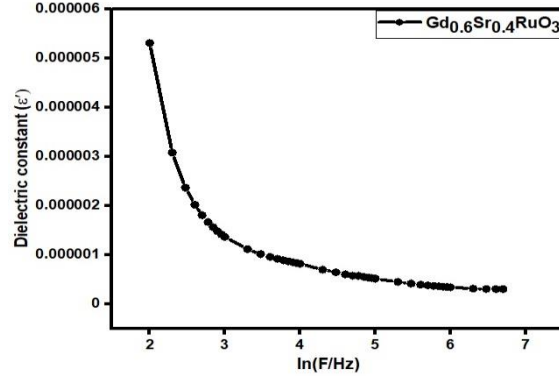
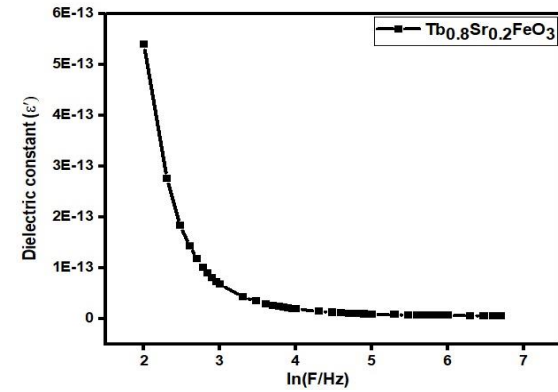
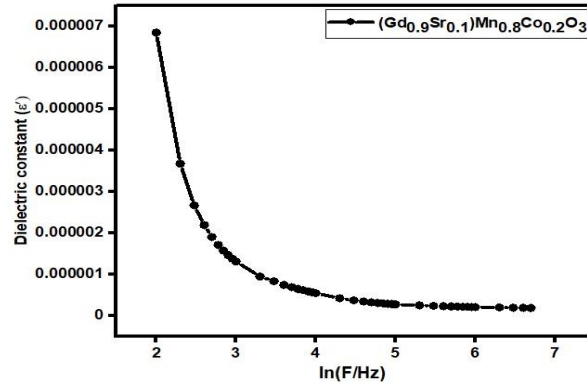
#### 2.2.4. Dielectric studies

Fig. 8 (a) and (b) show the effect of frequency (ln F/Hz) on the dielectric constant ( $\epsilon'$ ) and the dielectric loss factor ( $\tan \delta$ ) of the synthesized samples such as (Gd<sub>0.9</sub>Sr<sub>0.1</sub>) Mn<sub>0.8</sub>Co<sub>0.2</sub>O<sub>3</sub>, Tb<sub>0.8</sub> Sr<sub>0.2</sub>FeO<sub>3</sub>, Gd<sub>0.6</sub>Sr<sub>0.4</sub>RuO<sub>3</sub>, SrCe<sub>0.95</sub>Y<sub>0.05</sub>O<sub>3</sub>, and Mn<sub>0.6</sub>Co<sub>0.4</sub>SnO<sub>3</sub> at the room temperature. The values of dielectric constant decreases continuously with increasing frequency (see Fig. 8(a)) and this may be due to the combined contribution from ionic, space charge, electronic and interfacial polarizations. However, in the high – frequency region (> ln 5Hz), the variation of dielectric constant ( $\epsilon'$ ) is very much low with the increasing frequency. The variation of dielectric constant with frequency (ln F/Hz) is well understood by the Maxwell-Wagner model [60]. Accordingly to this model, any dielectric material is made up of two differently conducting layers, first layer being a conducting grains and other being isolated by grain boundaries that are poor conductors. The electric

field in a dielectric material can stimulate the migration of charge carriers or mobile ions. However these charge carriers get accumulated at the interface region of the grain-grain boundary due to their different conducting natures. Thus, the accumulation of charge carriers can lead to polarization which in turn leads to the dielectric constant ( $\epsilon'$ ). In literature, for the nanocrystalline regime, the grains and grain boundaries are large in number than the microcrystalline regime and they are found more complex in lower and higher frequencies, respectively in nano materials [61, 62]. At low frequencies region, the mobile charge carriers / oxygen ions in the substituted perovskite are free to align towards the applied electric field due to sufficient time available and migrate through grains and grain boundaries. These mobile charges get accumulated at the grain-grain boundary interface and therefore more dielectric constant ( $\epsilon'$ ) is shown by the nanocrystalline substituted perovskites. With the increase in frequency (in Hz) of the applied field, the mobile charge carriers gradually lose their ability to follow the field and become stagnant at one point of time. This leads to decrease the value of total dielectric constant ( $\epsilon'$ ) and remain constant at higher frequencies for these substituted perovskites.

The frequency (ln F / Hz) - dependent dielectric loss ( $\tan \delta$ ) of these substituted perovskite at room temperature are presented in Fig. 8 (b). The value of loss tangent ( $\tan \delta$ ) depends on many factors like structured homogeneity, stoichiometry and synthesis procedure. Also  $\tan \delta$  represents the difference in phase between the applied electric field and the current induced in the dielectric material. Similar to dielectric constant ( $\epsilon'$ ), the dielectric loss in substituted perovskites decreases at a higher rate (up to ln 4.5 Hz) with the increasing frequency and the rate is relatively very low beyond a certain

**A**



**B**

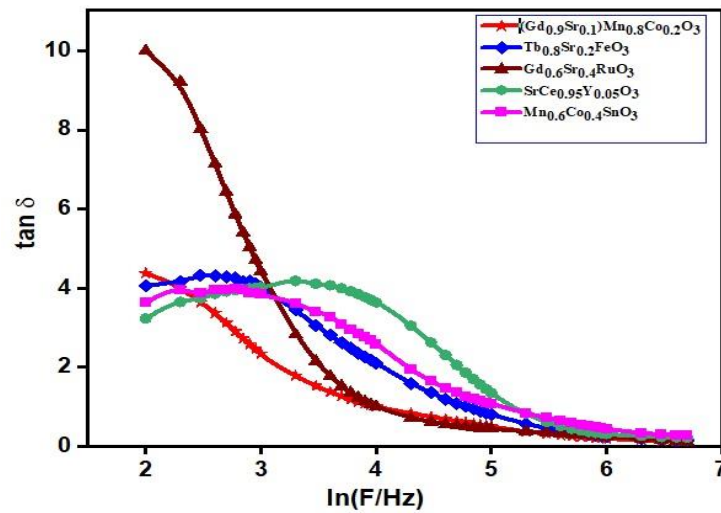


**Fig. 8.** Plot of variation of dielectric constant ( $\epsilon'$ ) with frequency (A) and dielectric loss ( $\tan \delta$ ) with frequency (B) of nanosized substituted perovskite compounds.

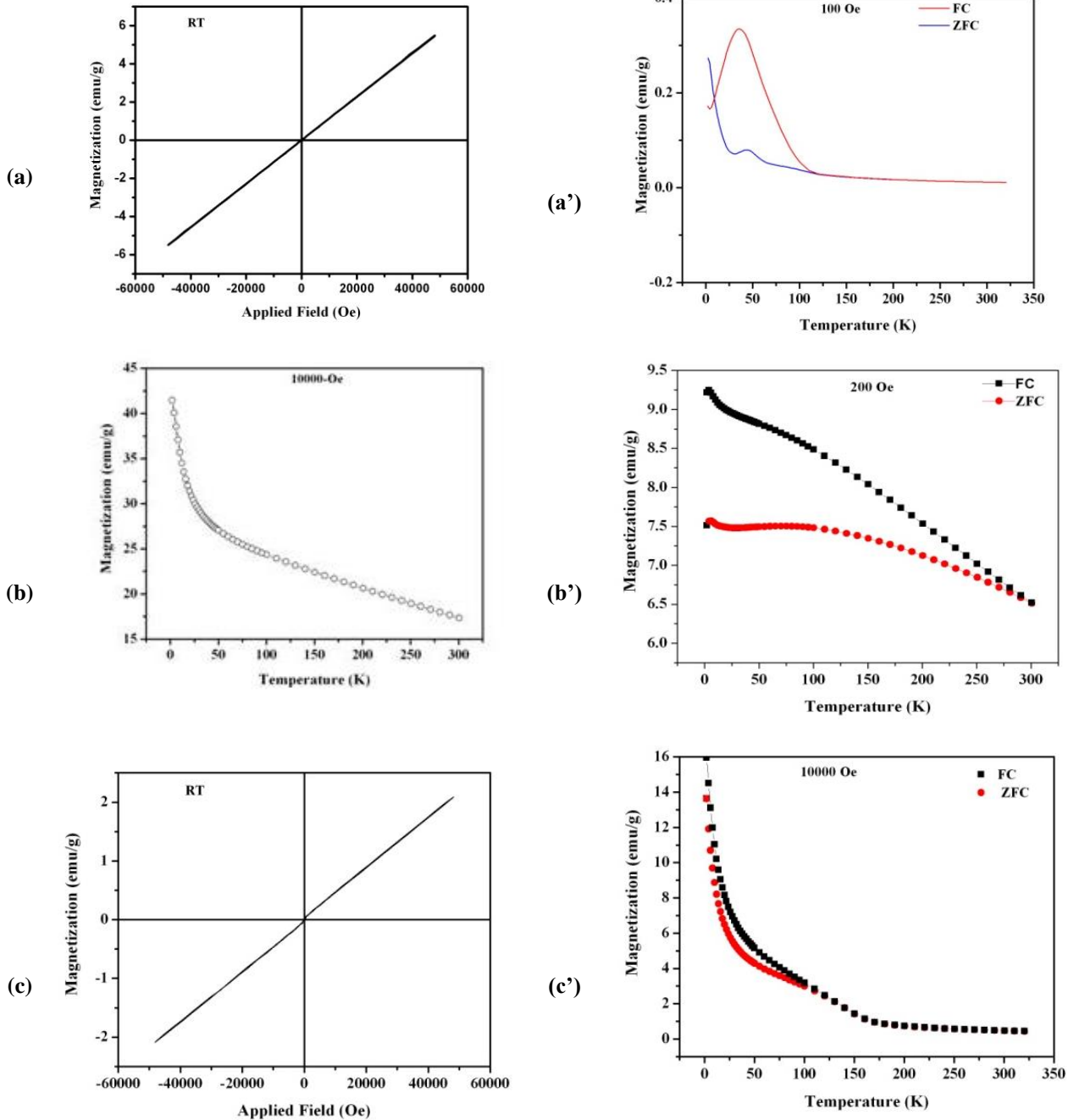
frequency (see Fig. 8(b)). At low-frequency region,  $\tan \delta$  have high value and more or less stable at the high-frequency region. This dispersion of dielectric loss with frequency is related to Koop's phenomenological theory, similar to the Maxwell-wagner model [63]. At low frequency region, which corresponds to high resistivity (due to grain boundaries) more energy required for electron exchange between  $M^{2+}$  and  $M^{3+}$  ions; thus the  $\tan \delta$  loss is high. In the high frequency range which corresponds to low resistivity (due grain) less is needed for electron transfer between  $M^{3+}$  to  $M^{2+}$  in the grains and

hence the  $\tan \delta$  is small. Therefore, at higher frequencies exhibit a constant  $\tan \delta$ , which suggest all samples possess a loss nature. This suggests all substituted perovskites could be utilized in high frequency device applications.

### 2.2.5 Magnetic studies

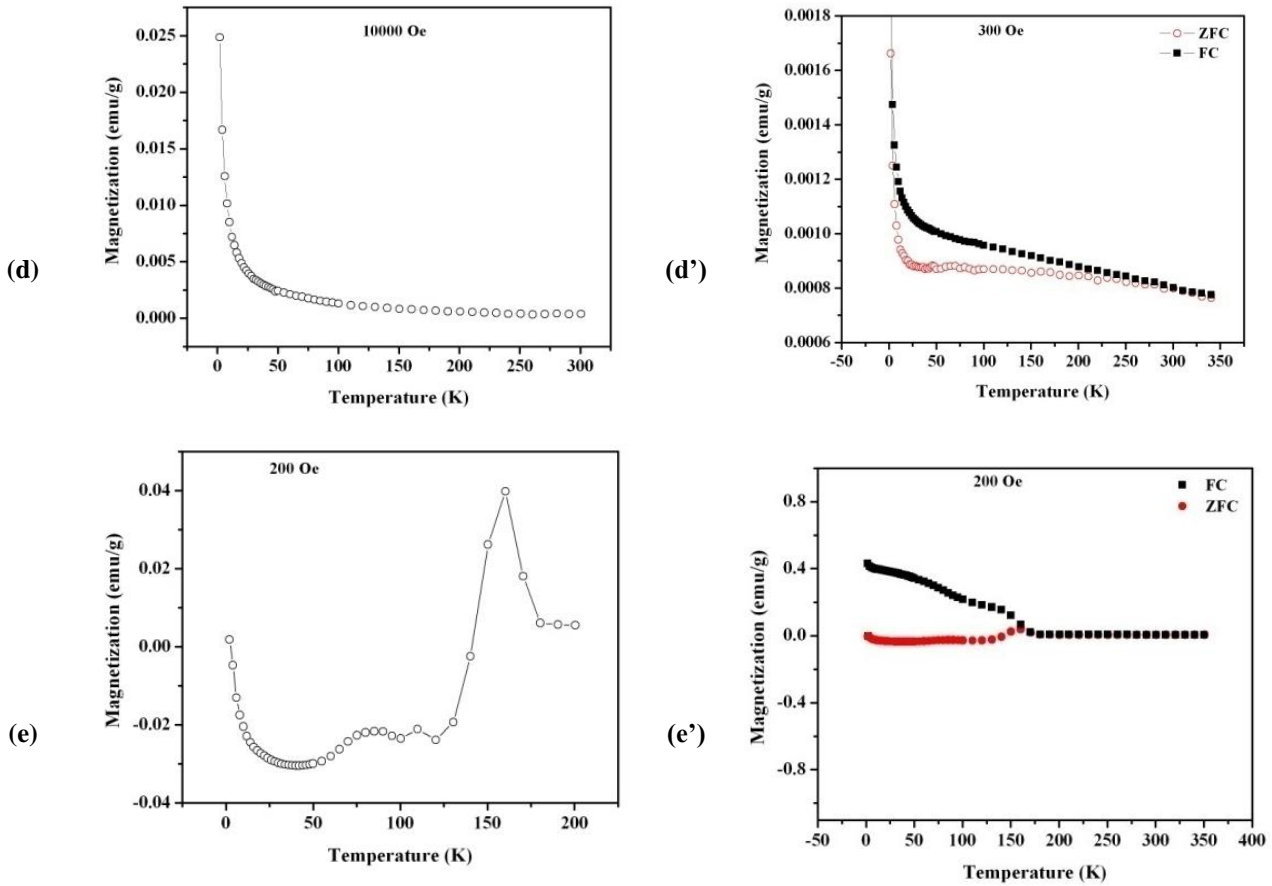
#### (a) For $(Gd_{0.9}Sr_{0.1})Mn_{0.8}Co_{0.2}O_3$

Fig. 9(a) shows the results of magnetization against the applied field measurement of  $(Gd_{0.9}Sr_{0.1})Mn_{0.8}Co_{0.2}O_3$  sample at room temperature. A very narrow hysteresis



**Fig. 9.** Magnetization Vs Applied field and ZFC and FC magnetization Vs temperature of nanosized substituted perovskite compounds.

(a)  $(Gd_{0.9}Sr_{0.1})Mn_{0.8}Co_{0.2}O_3$ , (b)  $Tb_{0.8}Sr_{0.2}FeO_3$ , (c)  $Gd_{0.6}Sr_{0.4}RuO_3$ ,



**Fig.9.** Magnetization Vs Applied field and ZFC and FC magnetization Vs temperature of nanosized substituted perovskite compounds. (d) SrCe<sub>0.95</sub>Y<sub>0.05</sub>O<sub>3</sub>, (e) Mn<sub>0.6</sub>Co<sub>0.4</sub>SnO<sub>3</sub>.

loop has been observed, suggesting the sample's ferromagnetic nature. For this sample, the remanent magnetization and coercive force could not be properly calculated from the hysteresis loop. It should be noted that even after applying a magnetic field of 60000 Oe (or 6T); the magnetization value did not show saturation. In the sample, this shows the existence of magnetic relaxation. The explanation for not having a saturated value of magnetization may be the very fine particles (nano size) present in the sample undergoing superparamagnetic relaxation at room temperature. Another reason is that the absence of saturation in the high field magnetization (6T) indicates a spin-canted ferromagnetic state in this sample (i.e. antiferromagnetic exchange coupling between Gd<sup>3+</sup> and Mn<sup>3+</sup>- Mn<sup>4+</sup> sublattice [64].

For (Gd<sub>0.9</sub>Sr<sub>0.1</sub>) Mn<sub>0.8</sub>Co<sub>0.2</sub>O<sub>3</sub> samples, the temperature dependence of magnetization of field-cooled (FC) and zero field-cooled (ZFC) measured at 100 Oe by a SQUID magnetometer is shown in Fig. 9 (a'). This sample shows relatively soft ferromagnets, with a rapid increase in magnetization occurring at a decreasing temperature. For this sample, the Curie temperature T<sub>c</sub> is determined from magnetization curves at 150 K. Thermal irreversibility Magnetization of FC > ZFC is observed below 156 K at 100 Oe. The FC is separated from the ZFC due to the presence of an anisotropy arising from ferromagnetic clusters. This feature is widespread in unconventional ferromagnets, such as magnetic

perovskites [65, 66]. In other words, there is a large discrepancy between ZFC and FC curve below T<sub>c</sub> which may imply a complex magnetic state after the magnetic ordering transition. This is due to the localizing influence of A-site of perovskite cation disorder is a more prominent factor than the average cation sizes < R<sub>A</sub> > that would enhance the double-exchange mediated ferromagnetism. On Sr<sup>2+</sup> substituting causes the broadening and shift to lower temperature magnetization. This is related to the mismatch factor (σ<sup>2</sup>) causes a decrease of T<sub>c</sub>, which inhibits charge more strongly than it affects the ferromagnetic double exchange to the disorder in the lattice of the perovskite phase. This compound has plateaued in field-cooled (FC) curve response at the temperature 145 K to 100 K, followed by a steady rise down to 35 K and finally a decrease in magnetization below 35 K (see Fig. 9(a')). The magnetization of this sample first goes from paramagnetic to ferromagnetic phase followed by the charge-ordered antiferromagnetic phase coexist. It is also seen in Fig. 9 (a') that a decrease in magnetization of ZFC much below the ferromagnetic ordering temperature and a continuously increasing magnetization of FC, when measured at low magnetic fields (100 Oe), have also been observed for other ferromagnetic systems showing long-range ferromagnetic order much below the temperature at which a drop in magnetization of ZFC is observed [67]. Such change in the magnetic structure can be explained based on random distribution of Gd<sup>3+</sup> ions

i.e. disorder state results in the random magnetic potential on the Mn sublattice. So long-range ferromagnetic order in Mn–O–Mn is impossible, resulting in Mn–O–Mn cluster and the forming of the cluster-spin glass state. Because long-range ferromagnetic order is destroyed, the  $T_c$  is decreased and magnetization is weakened on  $Gd^{3+}$  or  $Sr^{2+}$  doping.

### (b) For $Tb_{0.8}Sr_{0.2}FeO_3$

To confirm the coexistence of ferromagnetic coupling and antiferromagnetic coupling, the temperature dependence of magnetization of the  $Tb_{0.8}Sr_{0.2}FeO_3$  sample at the high applied field (10 K Oe) is shown in Fig. 9(b). It is evident from this Figure that a paramagnetic contribution appears superimposed to the ferromagnetic one. This contribution is also present in  $M(H)$  curves making the evolution of the actual value of the saturation magnetization difficult. It clearly indicates that only a fraction of Fe atoms participate in ferromagnetism, the rest contribute to the observed paramagnetic signal or may even be antiferromagnetically coupled. The curves show a rapid decay of magnetization at the low-temperature regime reflecting that the paramagnetic behavior predominates at the low-temperature regions. These results indicate that the existence of a strong antiferromagnetic interaction between Fe ions in the sample. The estimated Neel temperature is observed at  $T_N = 87$  K. The large  $Tb^{3+}$  paramagnetic signal hinders the direct observation of iron ordering in the sample with higher  $Tb^{3+}$  content. However, such ordering can be inferred from two features (i)  $T_N$  is visible at low temperature for this compound and (ii) The out-of-phase component of magnetization a sharp rise at the same temperature  $T_N$ . Such behavior also found for  $T_N$  in related series, has been attributed to the large exchange coupling of  $Fe^{3+}$  ions and can be attributed to a small spin canting in the antiferromagnetically ordered state [68]. However, the magnetizations do not go to zero (see Fig. 9(b) and the hysteresis loop is not observed at 300 K. These results demonstrate that only a minor Fe spin is ferromagnetically coupled and the predominant Fe spins remain uncoupled or even antiferromagnetic coupled.

The temperature-dependent magnetization curve of the  $Tb_{0.8}Sr_{0.2}FeO_3$  sample in zero field cooled (ZFC) and field cooled (FC) conditions in an applied 200 Oe is shown in Fig. 9(b'). A nonzero difference between FC and ZFC curve indicates ferromagnetic ordering. By taking the difference between these two quantities (denoted as  $\Delta M = M(FC) - M(ZFC)$ ), para- and diamagnetic contribution to the magnetization can be subtracted, leaving only a measure of the hysteretic ferromagnetic regime. Simultaneously, a non-zero difference indicates the presence of hysteresis, i.e. ferromagnetic ordering. This strongly supports the bound magnetic polaron (BMP) model for ferromagnetism in solid [69]. According to this model, a donor spins of defects strongly correlating with  $Fe^{3+}$  within its orbit can mediate effective interactions between them based on a Heisenberg exchange Hamiltonian [69]. It can be also seen that ZFC and FC magnetization curves show a distinct irreversible behavior. The irreversible temperature ( $T_{irr}$ ) is observed at 300 K for this sample.

$T_{irr}$  is the temperature below which the ZFC and FC curve split. The reduction in particle size (i.e. nanoparticles) causes in  $T_{irr}$  towards lower temperature.

### (c) For $Gd_{0.6}Sr_{0.4}RuO_3$

Fig. 9(c) shows the magnetization as a function of the applied field corresponding to the  $Gd_{0.6}Sr_{0.4}RuO_3$  sample at room temperature. The sample shows a clear narrow hysteresis loop with less coercivity, but certainly, it is still strongly ferromagnetic. It may be noted the magnetization value did not show saturation even after applying a magnetic field of 6 T. This indicates the presence of magnetic relaxation in the sample and is believed to be governed by antiferromagnetic interaction due to high magnetic ion ( $Ru^{3+}$ ) in the system. The very fine particles present (nanosized) in the sample undergoing superparamagnetic relaxation at room temperature could be the reason for not getting a saturated value of magnetization.

We have also investigated the magnetic properties of this sample ( $Gd_{0.6}Sr_{0.4}RuO_3$ ) using a SQUID magnetometer in the temperature 5 - 325 K. The temperature dependence of magnetization is shown in Fig. 9(c'). The figure shows a plot of zero-field-cooled (ZFC) and field-cooled (FC) magnetization measurements performed on this material by applying a field of 100 Oe. It can be seen that with temperature decreasing this compound undergo a transition from paramagnetic to a ferromagnetic state. The Curie temperature  $T_c$  (defined as the temperature corresponding to an abrupt increase of magnetization) observed for this compound at 200 K. This sample shows a distinct splitting between ZFC and FC measurement implying the presence of a magnetic transition temperature. This sample also exhibits a peak in its magnetization curve at 100 K. A large number of  $Gd^{3+}$  paramagnetic signals hinder the direct observance of ruthenium ordering in the sample [68]. Above  $T_c$ , the magnetization variation in the  $Gd_{0.6}Sr_{0.4}RuO_3$  system obeys the Curie-Weiss law. The obtained effective paramagnetic moments reasonably agree with the sum of contribution expected from Gd and Ru ions. Both kinds of Ru ions ( $Ru^{3+}$  and  $Ru^{4+}$ ) are high spin state.

Also in this sample ( $Gd_{0.6}Sr_{0.4}RuO_3$ ), when  $Sr^{2+}$  is substituted for  $Gd^{3+}$ , its larger size and lower charge enable it to compete more strongly for oxygen electrons. At the same time, the  $Ru^{3+}$  resulting from the substitution are less strongly bonded than the  $Ru^{4+}$ , because of its larger size and smaller charge. These effects are additive (i.e. superexchange interaction) both leading to a decreasing Ru–O interaction and presumably a narrower  $\pi^*$ -bond. This effect is quantified by the influence of tolerance factor ( $t$ ) on the superexchange interaction. This tolerance factor ( $t$ ) is listed in Table III. For a perfect size match,  $t = 1$ , the Ru–O–Ru bond angle ( $\theta$ ) would be  $180^\circ$ . For  $t < 1$  rather than a simple contraction of the bond distance, the octahedral tilt and resulting in  $\theta < 180^\circ$ . Thus the apparent decrease in tolerance factor ( $t$ ) with decreasing  $\theta$  for Ru – O – Ru bond angle at B-site of perovskite. At  $Gd_{0.6}Sr_{0.4}RuO_3$ , the bandwidth has been sufficiently decreased so that antiferromagnetic behavior is observed for this sample.

**(d) For SrCe<sub>0.95</sub>Y<sub>0.05</sub>O<sub>3</sub>**

The temperature dependence of magnetization at a high applied field (10 K Oe) for the SrCe<sub>0.95</sub>Y<sub>0.05</sub>O<sub>3</sub> sample is shown in Fig. 9 (d). There is an increase in magnetization because of oxygen vacancies in the sample. It is well known that cerium in SrCe<sub>0.95</sub>Y<sub>0.05</sub>O<sub>3</sub> can be Ce<sup>3+</sup> or Ce<sup>4+</sup> valence states. So the substitution of a rare-earth ion such as Y<sup>3+</sup> should create oxygen vacancies [70] and finally enhance the ferromagnetism. Thus, the appearance of such behavior is due to increasing the cation size at the A-site of perovskite, which inhibits charge ordering more strongly than it affects the ferromagnetic double exchange to the disorder in the lattice of the perovskite phase.

Ferromagnetic features are also found in the SrCe<sub>0.95</sub>Y<sub>0.05</sub>O<sub>3</sub> sample by studying the temperature dependence of magnetization after a ZFC-FC process under an applied field of 100 Oe (Fig. 9 (d')). ZFC curve is obtained by initially cooling the sample from 325 to 5 K in the absence of magnetic field and heating up in 100 Oe field while recording magnetization. For the FC measurements, the sample is cooled in the same field, and magnetization is recorded while heating up (FC). It is observed that the Curie transition temperature (T<sub>c</sub>) of this sample is above 350 K. As in the case of the sample, the magnetization against the temperature curve show irreversibility between the ZFC and FC curves due to the blocking process of superparamagnetic particles. It is worth noting that at low temperature (~ 30 K), the steep rise in magnetization seems to be intrinsic to diluted magnetic oxide, and also indicates that the presence of a paramagnetic phase at low temperature. In addition, since the particle is in the nano regime, some of the particles could behave superparamagnetically and the two contributions (paramagnetism and superparamagnetism) may complicate the magnetic behavior at low temperatures.

**(e) For Mn<sub>0.6</sub>Co<sub>0.4</sub>SnO<sub>3</sub>**

The temperature dependences of magnetization of Mn<sub>0.6</sub>Co<sub>0.4</sub>SnO<sub>3</sub> taken during heating in a magnetic field 200 Oe is shown in Fig.9 (e). The magnetization of this sample exhibits a sharp peak at 160 K, an abrupt decrease of the moment below this temperature then remains constant up to 75 K and a step like an upturn at a lower temperature (~ 20 K). The anomalies of physical properties at T<sub>c</sub> = 160 K in this sample are due to the transformation from the high-temperature paramagnetic state into the low-temperature antiferromagnetic state. There is the presence of a short-range magnetic interaction above the transition temperature T<sub>c</sub>. It has been argued that the presence of Mn<sup>3+</sup> (or Co<sup>3+</sup>) and Mn<sup>4+</sup> (or Co<sup>4+</sup>) ions and with spin-orbit coupling could be the source of the anisotropic nature of the ferromagnetic exchange interactions. While Sn<sup>4+</sup> is diamagnetic in this compound [36, 37]. The predominance of ferromagnetic exchange interaction in the high temperature would lead to the formation of the ferromagnetic state if the antiferromagnetic state had not occurred at T<sub>c</sub>. The over-cooled clusters are presumably present in the compound at low temperatures.

This is because the virtual Curie temperature in this compound practically coincides with the temperature of

the magnetic transition.

Fig. 9 (e') shows the temperature dependence of magnetization measured in an applied magnetic field of 200 Oe in both zero field cooled (ZFC) and field cooled (FC) modes for Mn<sub>0.6</sub>Co<sub>0.4</sub>SnO<sub>3</sub> sample. This compound shows large thermomagnetic irreversibility at applied (200 Oe). In ZFC and FC magnetization, branches were observed below the temperature T<sub>c</sub> = 150 K of gradual rise. The weak ferromagnetic ordering produced branching of ZFC and FC magnetization below T<sub>c</sub> (Fig. 9 (e')). The weak ferromagnetism is due to the canted antiferromagnetic interaction between Mn or Co ions via oxygen i.e. superexchange interaction.

Moreover, on cooling, antiferromagnetic interaction occurred at T<sub>c</sub> = 150 K for this compound underwent long-range antiferromagnetic ordering with weak ferromagnetism (corresponding to the gradual rises). This is the first observation in this compound. The difference in the onset of the antiferromagnetic ordering of this compound originates from the magnetic interaction between Mn or Co ions via oxygen, i.e., the Mn–O–Mn (or Co–O–Co) bond angle. The long-range antiferromagnetic ordering appeared at a higher temperature in this compound.

## Conclusions

1. The X-ray diffraction pattern of single-phase perovskite with orthorhombic structure For (Gd<sub>0.9</sub>Sr<sub>0.1</sub>)Mn<sub>0.8</sub>Co<sub>0.2</sub>O<sub>3</sub>, Tb<sub>0.8</sub>Sr<sub>0.2</sub>FeO<sub>3</sub>, Gd<sub>0.6</sub>Sr<sub>0.4</sub>RuO<sub>3</sub>, SrCe<sub>0.95</sub>Y<sub>0.05</sub>O<sub>3</sub> and Mn<sub>0.6</sub>Co<sub>0.4</sub>SnO<sub>3</sub> compounds, except Tb<sub>0.8</sub>Sr<sub>0.2</sub>FeO<sub>3</sub>Mn<sub>0.6</sub>Co<sub>0.4</sub>SnO<sub>3</sub> compounds, which showed cubic and rhombohedral structure respectively. The lattice parameter and unit cell volume slightly decrease as ionic radii decrease in agreement with the lanthanide contraction. The average size of cations < R<sub>A</sub> > of A-site of perovskite, mismatch factor (σ<sup>2</sup>), and tolerance factor (t) give combine effects of disorder and inhomogeneity in these perovskite compounds.

2. The temperature dependence of electrical conductivity for all substituted compounds show a definite break in 500 to 610 K except the Gd<sub>0.6</sub>Sr<sub>0.4</sub>RuO<sub>3</sub> compound, which corresponds to semiconducting behavior. While the Gd<sub>0.6</sub>Sr<sub>0.4</sub>RuO<sub>3</sub> sample shows a metallic-like semiconductor. The activation energy (E<sub>a</sub>) in the first region corresponds to the charge carriers are localized on the defect center, while E<sub>a</sub> in the second region corresponds to an intrinsic property of the compounds. Thermoelectric power and Hall effect measurement shows all compounds are n-type semiconductivity except SrCe<sub>0.95</sub>Y<sub>0.05</sub>O<sub>3</sub> compound, which show P-type semiconductivity.

3. Magnetic studies show the thermo-magnetic irreversibility for all substituted compounds. These compounds underwent long-range antiferromagnetic ordering with weak ferromagnetism in temperature dependence (5 - 325 K) of magnetization measurements. Enhanced ferromagnetism in most samples can be related to increased surface defects due to the nanosize of the powder.

### Acknowledgments

For their technical help during the SEM-EDAX and magnetization measurement experiment, the authors thank the staff of TIFR, Mumbai. They also thank DST-FIST Delhi, the staff of IIT Mumbai SAIF laboratories, for the ICPS and TEM-SAED experiments.

### Conflict of Interest Statement

On behalf of all authors the corresponding author states that there is no conflict of interest.

**M.B. Khanvilkar** – M.Sc.Ph.D, Associate Professor;  
**A.K. Nikumbh** – M.Sc.Ph.D, Professor;  
**R.A. Pawar** – M.Sc.Ph.D, Professor;  
**N.J. Karale** – M.Sc.Ph.D, Assistant Professor;  
**D.V. Nighot** – M.Sc.Ph.D, Associate Professor;  
**R.C. Ambare** – M.Sc.Ph.D, Assistant Professor;  
**P.A. Nagwade** – M.Sc.Ph.D, Assistant Professor;  
**M.D. Sangale** – M.Sc.Ph.D, Associate Professor;  
**G.S. Gugale** – M.Sc.Ph.D, Professor;  
**S.B. Misal** – M.Sc.Ph.D, Assistant Professor.

- [1] L. Zhang, J. Hu, P. Song, H. Qin, K. An, X. Wang and M. Jiang, *Sens. Actuators B* 119, 315 (2006), <https://doi.org/10.1016/j.snb.2005.12.030>.
- [2] J. Zosel, D. Franke, K. Ahiborn, F. Gerlach, V. Vashook and U. Guth, *Solid State Ionics* 179, 1628 (2008), <https://doi.org/10.1016/j.ssi.2008.01.044>.
- [3] C. R. Michel, E. Delgada, G. Santillan, A. H. Martynez and A. Chavez - Chavez, *Mat. Res. Bull.* 42, 84 (2007), <https://doi.org/10.1016/j.materresbull.2006.05.008>.
- [4] M.D. Gross, K.M. Carver, M.A. Deighan, A. Schenkel, B. M. Smith and A.Z. Yee, *J. Electrochem. Soc.* 156(4), 540 (2009), <https://doi.org/10.1149/1.3078406>.
- [5] T. Kolodiaznyi and A. Petric, *J. Electroceram.* 15, 5 (2005), <https://doi.org/10.1007/s10832-005-0375-7>.
- [6] P. Colomban, *Proton Conductors: Solids, Membranes and Gels - Materials and Devices* (Cambridge University Press, Cambridge, 1992), ISBN 0-521-38317-X.
- [7] K.D. Kreuer, *Chem. Mater.* 8, 610 (1996), <https://doi.org/10.1021/cm950192a>.
- [8] V.N. Stathopoulos, V.C. Blessi, and A.K. Ladavos, *React. Kinet. Catal. Lett.* 72(1), 49 (2001), <https://doi.org/10.1023/A:1010524312637>.
- [9] J.R. Mawdsley and T.R. Krause, *Appl. Catal. A* 334, 311 (2008), <https://doi.org/10.1016/j.apcata.2007.10.018>.
- [10] J. Cerda, J. Arbiol and G. Dezanneau, *Sens. Actuators B* 84, 21 (2002), [https://doi.org/10.1016/S0925-4005\(02\)00005-9](https://doi.org/10.1016/S0925-4005(02)00005-9).
- [11] A. Callaghan, C. W. Moeller and R. Ward, *Inorg. Chem.* 5, 1572 (1966), <https://doi.org/10.1021/ic50043a023>.
- [12] J. M. Longo, P. M. Racciah and J. B. Goodenough, *J. Appl. Phys.* 39, 1327 (1968), <https://doi.org/10.1063/1.1656282>.
- [13] H.Y. Hwang, S.W. Cheong, P.G. Radaelli, M. Marezio and B. Batlogg, *Phys. Rev. Lett.* 75, 914 (1995), <https://doi.org/10.1103/PhysRevLett.75.914>.
- [14] Khagesh Tanwar, Farheen Anjum, Ashutosh K. Shukla, and Tanmoy Maiti, *J. Appl. Phys.* 124, 094902 (2018), <https://doi.org/10.1063/1.5027125>.
- [15] Xiang Li, Chengliang Lu, Jiyan Dai, Shuai Dong, Yan Chen, Ni Hu, Guangheng Wu, Meifeng Liu, Zhibo Yan, and Jun-Ming Liu. *Scientific Reports*; <https://doi.org/10.1038/srep07019>.
- [16] G.H. Jonker and J.H. Vansanten, *Physica* 16, 337 (1950), [https://doi.org/10.1016/0031-8914\(50\)90033-4](https://doi.org/10.1016/0031-8914(50)90033-4).
- [17] P. Schiffer, A.P. Ramirez, W. Bao, and S. W. Cheong, *Phys. Rev. Lett.* 75, 3336 (1995), <https://doi.org/10.1103/PhysRevLett.75.3336>.
- [18] B. Raveau, A. Maignan and C. Martin, *J. Solid State Chem.* 130, 162 (1997), <https://doi.org/10.1006/jssc.1997.7373>.
- [19] M. Eibschutz, S. Shtrikman and D. Treves, *Phys. Rev.* 156, 562 (1967), <https://doi.org/10.1103/PhysRev.156.562>.
- [20] J.B. MacChesney, R.C. Sherwood and J.F. Potter, *J. Chem. Phys.* 43, 1907 (1965), <https://doi.org/10.1063/1.1697052>.
- [21] T. Takeda, K. Komura and H. Fujii, *J. Magn. Magn. Mater* 31, 797 (1983), [https://doi.org/10.1016/0304-8853\(83\)90690-X](https://doi.org/10.1016/0304-8853(83)90690-X).
- [22] Yiming Cao, Maolin Xiang, Weiyao Zhao, Guohua Wang, Zhenjie Feng, Baojuan Kang, Alessandro Stroppa, Jincang Zhang, Wei Ren, and Shixun Cao *J. Appl. Phys.* 119, 063904 (2016), <https://doi.org/10.1063/1.4941105>.
- [23] R.J. Bouchard and J.L. Gillson, *Mater. Res. Bull.* 7 (1972) 873, [https://doi.org/10.1016/0025-5408\(72\)90075-X](https://doi.org/10.1016/0025-5408(72)90075-X). R. J. Bouchard and J. F. Weiher, *J. Solid State Chem.* 4, 80 (1972), [https://doi.org/10.1016/0022-4596\(72\)90135-1](https://doi.org/10.1016/0022-4596(72)90135-1).
- [24] R. Greatrex, G. Hu and D.C. Munro, *Mater. Res. Bull.* 21, 797 (1986), [https://doi.org/10.1016/0025-5408\(86\)90164-9](https://doi.org/10.1016/0025-5408(86)90164-9).
- [25] J.M. Longo, P.M. Racciah and J.B. Goodenough, *J. Appl. Phys.* 39, 1327 (1968), <https://doi.org/10.1063/1.1656282>.

- [26] A. Callaghan, C.W. Moeller, and R. Ward, *Inorg - Chem.* 5, 1572 (1966), <https://doi.org/10.1021/ic50043a023>.
- [27] A. Labdelli, S. Meskine, A. Boukortt, and R. Khenata J. *New Technol. Mater.* 8, 126 (2018).
- [28] A. Kanbayashi, *J. Phys. Soc. Japan* 44, 108 (1978), <https://doi.org/10.1143/JPSJ.44.108>.
- [29] J. Guan, S.E. Dorris, U. Balachandran and M. Liu, *Solid State Ionics* 100, 45 (1997), [https://doi.org/10.1016/s0167-2738\(97\)00320-2](https://doi.org/10.1016/s0167-2738(97)00320-2).
- [30] U. Reiche, R.R. Arons and W. Schilling, *Solid State Ionics* 86-88, 639 (1996), [https://doi.org/10.1016/0167-2738\(96\)00228-7](https://doi.org/10.1016/0167-2738(96)00228-7).
- [31] T. Yajima, H. Kazeoka, T. Yogo, and J. Iwahara, *Solid State Ionics* 47, 271 (1991), [https://doi.org/10.1016/0167-2738\(91\)90249-B](https://doi.org/10.1016/0167-2738(91)90249-B).
- [32] K.S. Knight and N. Bonanos, *Solid State Ionics* 77, 189 (1995), [https://doi.org/10.1016/0167-2738\(94\)00271-S](https://doi.org/10.1016/0167-2738(94)00271-S).
- [33] M.J. Lopez-Robledo. C. Vaquero – Aguilar, J. Martinez - Fernandez, J. I. Pena, A. Sayir and M. Jimenez - Melendo, *J. Eur. Ceram. Soc.* 31, 1339 (2011), <https://doi.org/10.1016/j.jeurceramsoc.2010.05.022>.
- [34] Glenn C. Mather, Filipe M. Figueiredo, Julio Romero de Paz, and Susana Garcia – Martin *Inorg. Chem.* 47, 921 (2008), <https://doi.org/10.1021/ic701703c>.
- [35] G. Haacke, H. Ando and W.E. Mealmaker, *Electrochem. Soc.* 124, 1923 (1977), <https://doi.org/10.1149/1.2133196>.
- [36] K. Leinenweber, W. Utsumi, Y. Tsuchida, T. Yagi and K. Kurita *Phys. Chem. Minerals* 18, 224 (1991), <https://doi.org/10.1007/BF00202576>.
- [37] O. Parkash, K.D. Mandal, C.C. Christopher et al., *J. Mater. Sci.* 31, 4705 (1996), <https://doi.org/10.1007/BF00366373>.
- [38] P.S. Bearmann, V. Thangadurai and W. Weppner, *J. Solid State Chem.* 174, 392 (2003), [https://doi.org/10.1016/S0022-4596\(03\)00258-5](https://doi.org/10.1016/S0022-4596(03)00258-5).
- [39] Sung Gu Kang, *J. Solid State Chem.*; <https://doi.org/10.1016/j.jssc.2018.03.026>.
- [40] V.T. Dinh, V.O. Mittova and I.Ya. Mittova, *Inorg. Mater.* 47(5), 521 (2011), <https://doi.org/10.1134/S0020168511050086>.
- [41] A.K. Nikumbh, A.V. Nagawade, G.S. Gugale, M.G. Chaskar, and P.P. Bakare, *J. Mater. Sci.* 37, 637 (2002), <https://doi.org/10.1023/A:1013790129045>.
- [42] K.N. Akamoto, *Infrared Spectra of Inorganic and Coordinated Compounds* (Wiley– Interscience, New York, Second Edition, 1970).
- [43] J.A. Allan, N.D. Baird and A.L. Kassyk, *J. Therm. Anal.* 16, 79 (1979), <https://doi.org/10.1007/BF01909635>.
- [44] R.H. Nattal and G.A. Melson, *J. Inorg. Nucl. Chem.* 25, 2979 (1969).
- [45] M. Khorasami - motlagh, M. Noroozifar, M. Yousefi and S. Jahani *Int. J. Nanosci. Nanotechnol.* 9(1), 7 (2013); (b) W. Cui, F. Wang, J. Wang and Y. Xia, *Electrochimica Acta* 56, 4812 (2011), <https://doi.org/10.1016/j.electacta.2011.03.006>.
- [46] JCPDS File No 250337.
- [47] JCPDS File No.400905.
- [48] JCPDS File No.010821469.
- [49] JCPDS File No.010831157.
- [50] JCPDS File No.010850864, (b) Y. Syono, H. Sawamoto and S. Akimoto, *Solid State Communications* 7, 713 (1969), [https://doi.org/10.1016/0038-1098\(69\)90600-0](https://doi.org/10.1016/0038-1098(69)90600-0).
- [51] L.M. Rodriguez-Martinez and J.P. Attfield, *Phys.Rev B* 54(22), R15622 (1996), <https://doi.org/10.1103/PhysRevB.54.R15622>.
- [52] Y. Tomioka and Y. Tokura, *Phys.Rev. B* 70, 14432 (2004), <https://doi.org/10.1103/PhysRevB.70.014432>.
- [53] R.D. Shanon, *Acta Crystallogr.* 32, 751.153 (1976), <https://doi.org/10.1107/S0567739476001551>.
- [54] X. Liu and C.T. Pewitt, *J. Phys. Chem. Solids* 52, 441 (1991), [https://doi.org/10.1016/0022-3697\(91\)90097-J](https://doi.org/10.1016/0022-3697(91)90097-J).
- [55] D. Louca, J.L. Sarrao, J.D. Thopson, H. Roeder and G.H. Kwei, *Phys.Rev.B* 60, 376 (1999), <https://doi.org/10.1103/PhysRevB.60.10378>.
- [56] L.M. Rodriguez-Martinez and J. P. Attfield, *Phys.Rev. B* 58, 2426 (1998), <https://doi.org/10.1103/PhysRevB.58.2426>.
- [57] D. Emin and T. Holstein, *Ann. Phys. Spectros.* 24, 436 (1970), [https://doi.org/10.1016/0003-4916\(69\)90034-7](https://doi.org/10.1016/0003-4916(69)90034-7).
- [58] J. Paul, *Attfeld. Chem. Mater.* 10, 3239 (1998), <https://doi.org/10.1021/cm980221s>.
- [59] G. Geller, *J. Chem.Phys.* 24, 1236 (1956), <https://doi.org/10.1063/1.1742746>.
- [60] J.C. Maxwell, *Electricity and Magnetism* vol. I (Oxford University Press England) 828 (1973); (b) K.W. Wangner, *Am. phys* 40, 817 (1973).
- [61] K.C. Verma, M. Ram, J. Singh and R.K. Kotnala, *J. Alloy. Compd.* 509, 4967 (2011), <https://doi.org/10.1016/j.jallcom.2011.01.144>.
- [62] C. Kaliyaperumal, S. Jayabalan, A. Sankarakumar and T. Paramasivam, *Solid State Sci.* 105, 106245 (2020), <https://doi.org/10.1016/j.solidstatesciences.2020.106245>.

- [63] C.G. Koops, Phys. Rev. 83, 121 (1951), <https://doi.org/10.1103/PhysRev.83.121>.
- [64] G.J. Snyder, C.H. Booth, F. Bridges, R. Hiskes, S.Di Carolis, M.R. Beasley and T.H. Geballe, Phys.Rev.B 55, 6453 (1997), <https://doi.org/10.1103/PhysRevB.55.6453>.
- [65] D.A. Filippov, K.V. Klimov, R.Z. Levitin, A.N. Vasilev, T.N. Voloshok and R. Suryanarayanan, J. Phys. Condens. Matter 15, 8351 (2003), <https://doi.org/10.1088/0953-8984/15/49/013>.
- [66] T.L. Phan, S.C. Yu, N.V. Khiem, M.H. Phan, J.R. Rhee, N.X. Phuc. J. Appl. Phys. 97, 10A508 (2005), <https://doi.org/10.1063/1.1855197>.
- [67] Z. Sun, H. Zhang, J. Wang and B. Shen, J. Appl. Phys. 86, 5152 (1999), <https://doi.org/10.1063/1.371492>.
- [68] S.K. Park, T. Ishikawa, Y. Tokura, J.Q. Li and Y. Matsui, Phys.Rev .B 60, 10788 (1999), <https://doi.org/10.1103/PhysRevB.60.10788>.
- [69] J.M.D. Coey, M. Venkatesan and C.B. Fitzgerald, Nat. Mater.4, 173 (2005), <https://doi.org/10.1038/nmat1310>.
- [70] J.R. McBride, K.C. Hass, B.D. Poindexter and W.H. Weber, J. Appl. Phys. 76, 2435 (1994), <https://doi.org/10.1063/1.357593>.

М.Б. Ханвілкар<sup>1,2</sup>, А.К. Нікумбх<sup>1</sup>, Р.А. Павар<sup>1</sup>, Н.Й. Карале<sup>1</sup>, Д.В. Нігхот<sup>1</sup>,  
Р.С. Амбаре<sup>2</sup>, П.А. Нагуаде<sup>1</sup>, М.Д. Сангал<sup>1</sup>, Г.С. Гугал<sup>1</sup>, С.Б. Місал<sup>1</sup>

## Отримання та характеристика нанорозмірних заміщених сполук перовскіту ромбічної структури

<sup>1</sup>Кафедра хімії, Savitribai Phule Pune University (колишній Університет Пуни), Ганешхінд, Пуна, Індія, [mb.khanvilkar@gmail.com](mailto:mb.khanvilkar@gmail.com)

<sup>2</sup>Коледж 2К.М.С., Хополі, Тал-Халанур, Dist. Райгад, Індія, [revanambare@gmail.com](mailto:revanambare@gmail.com)

Синтезовано п'ять заміщених перовскітів ( $Gd_{0.9}Sr_{0.1}Mn_{0.8}Co_{0.2}O_3$ ,  $Tb_{0.8}Sr_{0.2}FeO_3$ ,  $Gd_{0.6}Sr_{0.4}RuO_3$ ,  $SrCe_{0.95}Y_{0.05}O_3$ , and  $Mn_{0.6}Co_{0.4}SnO_3$ ) та попередньо додано прекурсори тартрату та гідроксиду. Отримані зразки досліджені за допомогою спектроскопії індуктивно зв'язаної плазми, енергодисперсійного рентгенівського аналізу, інфрачервоної спектроскопії, термічного аналізу, рентгенівської порошкової дифракції, просвічуючого електронного мікроскопа (ТЕМ), виділеного поля дифракції електронів (SAED) при постійному струмі, досліджено електропровідність, ефект Холла, проведено діелектричні вимірювання та вимірювання низькотемпературної намагніченості. На рентгенограми для всіх сполук показано утворення однофазного перовскіту із ромбічною структурою, крім перовскітів  $Tb_{0.8}Sr_{0.2}FeO_3$  та  $Mn_{0.6}Co_{0.4}SnO_3$ . Ці сполуки мали кубічну та ромбоєдричну структуру, відповідно. Параметр ґратки та об'єм елементарної комірки дещо зменшилися у міру зменшення іонних радіусів, відповідно до скорочення лантанодів. Середній розмір катіона  $\langle RA \rangle$ , коефіцієнт невідповідності ( $\sigma_2$ ) і коефіцієнт толерантності ( $t$ ) дають сукупні ефекти безладу та неоднорідності в цих сполуках. Середній розмір частинок, визначений за допомогою ТЕМ, був у діапазоні від 22 до 77 нм для всіх сполук. Були обрані різні площини решітки в шаблоні SAED, які узгоджувалися з монокристалографічною фазою цих перовскітів. Температурна залежність електропровідності для всіх сполук показала певний розрив від 500 К до 610 К. за винятком сполуки  $Gd_{0.6}Sr_{0.4}RuO_3$ , що відповідає напівпровідниковій поведінці. Тоді як зразок  $Gd_{0.6}Sr_{0.4}RuO_3$  демонструє металоподібний напівпровідник. Вимірювання термоелектричної потужності та ефекту Холла для всіх сполук вказали на напівпровідники n-типу, за винятком сполуки  $SrCe_{0.95}Y_{0.05}O_3$ , де отримано р-тип. Частотну залежність діелектричної проникності та діелектричних втрат у цих заміщених перовскітах обговорено за допомогою моделі Максвелла-Вагнера. Магнітні дослідження показали термомагнітну (вимірювання ZFC і FC) незворотність для всіх сполук.

**Ключові слова:** нанорозмірний заміщений перовскіт, феромагнетизм, електропровідність, намагніченість, обмінна взаємодія.